J. Mech. Phys. Solids 185 (2024) 105549

Contents lists available at ScienceDirect

Journal of the Mechanics and Physics of Solids

journal homepage: www.elsevier.com/locate/jmps

Temperature-dependent, multi-mechanism crystal plasticity reveals the deformation and failure behaviour of multi-principal element alloys

Yilun Xu [a,d,*], Xiaochong Lu [b,c,*], Xinyu Yang [a], Wanghui Li [a], Zachary Aitken [a], Guglielmo Vastola [a], Huajian Gao [a,c,e], Yong-Wei Zhang [a,*]

[a] Institute of High Performance Computing (IHPC), Agency for Science, Technology and Research (A*STAR), 1 Fusionopolis Way, #16-16 Connexis, Singapore 138632, Republic of Singapore
[b] School of Aeronautics and Astronautics, Sichuan University, Chengdu 610065, PR China
[c] School of Mechanical and Aerospace Engineering, Nanyang Technological University, Singapore 639798, Singapore
[d] Department of Materials, Imperial College, London SW7 2AZ, UK
[e] Center for Advanced Mechanics and Materials, Applied Mechanics Laboratory, Department of Engineering Mechanics, Tsinghua University, 100084 Beijing, China

ARTICLE INFO

Keywords:
Crystal plasticity
Multi-principal element alloys
Stored energy density
Short-range ordering

ABSTRACT

In this work, we have developed a temperature-dependent, multi-mechanism crystal plasticity (CP) model aimed at unravelling the deformation and failure resistance of Cantor alloy-like multi-principal element alloys (MPEA) under both uniaxial tensile and cyclic loading conditions. Three deformation mechanisms: dislocation slip, deformation twinning, and phase transformation are considered under a unified stress-driven, thermally activated law. In addition, the effect of short-range ordering (SRO) is introduced by accounting for the inhomogeneous distributions of material properties within individual grains. Our work yields the following key findings: (1) The rate- and temperature-sensitivity of the materials, such as the occurrence and sequence of dislocation slip, deformation twinning, and martensitic phase transformation observed in experiments can be captured through the calibrated material properties. (2) The enhancement of the mechanical response of the Cantor alloy-like MPEAs due to the SRO effect is intrinsically linked to the generation of geometrically necessary dislocations resulting from localized variations in material properties. (3) The excellent fatigue and fracture resistance exhibited by Cantor alloy-like MPEAs at low temperatures can be attributed to the homogenization of stored energy density within the microstructure. This homogenization arises from the development of deformation twinning and martensitic phase transformation. Our newly developed CP model and the key findings provide a valuable guide for the design of MPEAs to achieve superior fatigue and fracture resistance without compromising their inherent strength.

1. Introduction

Multi-principal element alloys (MPEAs), also known as high/medium-entropy alloys (HEAs or MEAs), have been a focus within the

* Corresponding authors.
E-mail addresses: yilun.xu@imperial.ac.uk (Y. Xu), luxiaochong@scu.edu.cn (X. Lu), zhangyw@ihpc.a-star.edu.sg (Y.-W. Zhang).

https://doi.org/10.1016/j.jmps.2024.105549
Received 5 December 2023; Received in revised form 10 January 2024; Accepted 10 January 2024
Available online 13 January 2024

research and engineering community of alloys due to their excellent material performance (George et al., 2019). Notably, MPEAs have demonstrated the ability to overcome the longstanding strength-ductility trade-off commonly associated with metallic materials (Li et al., 2016). As a pioneering benchmark among MPEAs, the single-phase, equiatomic, CrMnFeCoNi alloy, often referred to as the Cantor alloy, was first developed by Cantor (Cantor et al., 2004). Experimental evidence has consistently demonstrated its remarkable damage resistance, particularly at extremely low temperatures (Cantor, 2021; Gludovatz et al., 2014, 2016; Liu et al., 2022), which outperforms other alloys, including superalloys. The improved fracture and fatigue resistance of the Cantor alloy can be attributed to prolonged plasticity resulting from a specific sequence of deformation mechanisms, including dislocation slip, deformation twinning and martensitic phase transformation from face-centred cubic (FCC) to hexagonal close packed (HCP). These mechanisms have been found to be strongly temperature-dependent. Currently, there is no mechanistic grain-scale model that can be used to explore the temperature-dependent, multi-mechanism deformation in the Cantor-like MPEAs. To bridge this critical gap in the existing body of research, the present work aims to formulate a temperature-dependent, multi-mechanism deformation crystal plasticity model so as to provide valuable insights into the deformation and failure behaviour of MPEAs, particularly those similar to the Cantor alloy.

Grain-scale deformation plays a pivotal role in unravelling the macroscopic performance characteristics of MPEAs, including crucial factors such as strength, ductility, and damage resistance. Crystal plasticity finite element (CPFE) method is a suitable approach to describe the local anisotropic deformation of alloys at the grain scale, as it considers various deformation mechanisms (Roters et al., 2010), including dislocation slip, twinning and phase transformation. Among these deformation mechanisms, the constitutive laws for temperature-dependent dislocation slip have been well established (Dunne et al., 2007) and validated through rigorous experimental tests (Jiang et al., 2015; Zhang et al., 2022b). In contrast, when it comes to modelling deformation twinning and phase transformation in steels (Wong et al., 2016) and MPEAs (Lu et al., 2020b), most approaches rely heavily on phenomenological laws. This reliance often leads to complex constitutive equations and excessive fitting parameters, which can diminish the robustness of the models. Besides, it is difficult to unambiguously discern the impact of each individual mechanism as the constitutive laws and associated parameters are often formulated in different forms or derived from distinct physical origins.

Recently, SRO has been experimentally observed in MPEAs, including the Cantor alloy. Studies have indicated that SRO can substantially influence plastic deformation (Jian et al., 2020) and ductility (Chen et al., 2021a) of MPEAs. Existing studies (Li et al., 2022a) have rarely explored the SRO effect at the grain scale in modelling and, consequently, a comprehensive mechanistic understanding is still lacking. Therefore, there is a critical need for an SRO-incorporated, multi-mechanism CPFE framework that unifies the constitutive laws governing individual deformation mechanisms to accurately model the temperature-dependent mechanical response of MPEAs.

Damage development within crystalline materials, in terms of crack nucleation and propagation, has been experimentally demonstrated to be strongly dependent on the local microstructure and its length scale. Factors such as grain orientation, grain morphology and grain boundary character play a significant role in influencing this behaviour (Sangid, 2013; Sangid et al., 2011). It is important to note that the classical Paris law does not adequately account for the distinctive characteristics driven by the microstructure factors. Inspired by experimental evidence and Griffith energy concept, a microstructure-sensitive driver, namely the stored energy density (SED), has been proposed (Xu et al., 2021b) to predict crack nucleation and short crack propagation when the crack length falls in the grain size scale. The concept of SED takes into account the intrinsic dynamics of local dislocation slip during cyclic loading, which establishes a dislocation structure over a length scale governed by local dislocation density. The SED has been shown to be dominated by the distribution of geometrically necessary dislocations (GNDs) (Zheng et al., 2019), and hence, SED serves as a mechanistic measure for the energy stored within the material which, when reaching a critical level, will drive the initiation and propagation of new crack surfaces. The pioneering application of SED focused on predicting crack nucleation (Wan et al., 2014) in steels, which share similarities with MPEAs with multiple major elements. By highlighting the non-singularity of SED at the crack tip and providing the microstructural sensitivity from a theoretical deduction (Xu et al., 2021b), SED has been applied to understand fatigue crack nucleation in Nickel-based alloys (Zhang et al., 2021), Cu-based alloy (Qian et al., 2023), Sn-based alloy (Xu et al., 2022), Zr-based alloy (Wan et al., 2023), as well as short crack propagation in Nickel-based alloys (Karamitros et al., 2022) and Zr-based alloy (Long and Dunne, 2023). A similar energy measure, referred to as the dislocation configuration energy (Benzerga et al., 2005), which can be evaluated at the discrete dislocation scale, provides a physical interpretation that supports the validity of the SED approach. As damage accumulation in MPEAs primarily arises from deformation at the microstructure scale driven by plastic activities (Lu et al., 2023), the SED is adopted in the present study to predict the damage accumulation within MPEAs subject to cyclic loading at different temperatures.

In this work, we aim at developing a multi-mechanism crystal plasticity model for Cantor alloy-like MPEAs in which the three deformation mechanisms (dislocation slip, deformation twinning, and phase transformation) are formulated under a unified framework. In addition, we also incorporate the effects of SRO and temperature into the model, enabling the examination of their impacts on the mechanical behaviour of the MPEAs. Finally, we employ the developed model to unveil the underlying origin for the superior damage resistance of the Cantor alloy-like MPEA at extremely low temperatures.

The structure of the present paper is organized as follows: In Section 2, we describe our CPFE framework, which incorporates multiple deformation mechanisms, temperature effect and SRO phenomenon. This section also describes the associated representative volume element (RVE) models and the critical aspect of SED. In Section 3, we present an in-depth exploration of the temperature-dependent mechanical behaviour of the multiple principal element alloy (MPEA) subject to monotonic loading and cyclic loadings at three typical testing temperatures. In Section 4, we encapsulate our study with a concise summary and concluding remarks.

2. Methodology

2.1. The crystal plasticity framework

A multi-mechanism, dislocation-based CPFE framework that incorporates the local SRO effect is proposed to describe the mechanical behaviour of Cantor alloy-like MPEAs, where the deformation mechanisms include dislocation slip, deformation twinning and martensitic phase transformation. The model formulations are detailed in Section 2.1.1. The SRO effect is introduced into the CPFE framework through local fluctuations of mechanical properties within grains; for details see Section 2.1.2.

2.1.1. A crystal plasticity framework incorporating thermally activated dislocation slip, twinning and phase transformation

During deformation, the overall deformation gradient **F** at a material point is decomposed into three terms: the elastic deformation gradient $\mathbf{F_e}$, the plastic deformation gradient $\mathbf{F_p}$ and the temperature deformation gradient $\mathbf{F_\theta}$, as:

$$\boldsymbol{F} = \boldsymbol{F}_e \boldsymbol{F}_p \boldsymbol{F}_{\boldsymbol{\theta}}. \tag{1}$$

The kinematics for multi-mechanism crystal plasticity takes into account the contribution of deformation twinning and phase transformation in addition to the dislocation slip (Lu et al., 2020b), which gives the overall plastic velocity gradient tensor $\mathbf{L_p}$:

$$\boldsymbol{L}_p = (1 - f_{tw} - f_{tr})\boldsymbol{L}_p^{(\alpha)} + \boldsymbol{L}_p^{(\beta)} + \boldsymbol{L}_p^{(\chi)}, \tag{2}$$

where $\mathbf{L_p}^{(\alpha)}$, $\mathbf{L_p}^{(\beta)}$ and $\mathbf{L_p}^{(\chi)}$ are the plastic velocity gradient tensors of dislocation slip, deformation twinning and phase transformation, respectively.

These velocity gradient tensors can be computed from the projection of the corresponding shear strain rate onto specific crystallographic systems as:

$$\boldsymbol{L}_p^{(\alpha)} = \sum_{\alpha=1}^{N_{ds}} \dot{\gamma}^{(\alpha)} \boldsymbol{m}_{ds}^{(\alpha)} \otimes \boldsymbol{n}_{ds}^{(\alpha)}, \boldsymbol{L}_p^{(\beta)} = \sum_{\beta=1}^{N_{tw}} \dot{\gamma}^{(\beta)} \boldsymbol{m}_{tw}^{(\beta)} \otimes \boldsymbol{n}_{tw}^{(\beta)}, \boldsymbol{L}_p^{(\chi)} = \sum_{\chi=1}^{N_{tr}} \dot{\gamma}^{(\chi)} \boldsymbol{m}_{tr}^{(\chi)} \otimes \boldsymbol{n}_{tr}^{(\chi)}, \tag{3}$$

where $\dot{\gamma}^{(\alpha)}$, $\dot{\gamma}^{(\beta)}$ and $\dot{\gamma}^{(\chi)}$ are the shear strain rates of dislocation slip, deformation twinning and phase transformation, respectively. The deformation systems are indicated by their plane normal and direction unit vectors as **m** and **n**. For instance, there are 12 potentially activated dislocation slip systems {111}<110> within a Face-Centred Body (FCC) crystal structure; e.g., see an illustration in (Prastiti et al., 2020).

In Eq. (2), f_{tw} and f_{tr} are the overall volume fraction of deformation twinning and martensitic phase transformation, respectively, which are given as:

$$\begin{aligned} f_{\mathrm{tw}} &= \sum_{\beta=1}^{N_{\mathrm{tw}}} f^{(\beta)}, \\ f_{tr} &= \sum_{\chi=1}^{N_{tr}} f^{(\chi)}, \end{aligned} \tag{4}$$

where $f^{(\beta)}$ and $f^{(\chi)}$ are the volume fractions, N_{tw} and N_{tr} the numbers of potential twinning and phase transformation systems, respectively. For an FCC crystal structure such as the Cantor alloy under investigation, there are 12 twinning and phase transformation systems sharing the same planes and directions {111}<211> (see Fig. A1 for the illustration). It is noted that phase transformation in the Cantor alloy-like systems is limited to the deformation process of the ε phase transformation (i.e. from FCC to HCP phase) only, following the experimental observation (Liu et al., 2022).

The shear strain rates of deformation twinning $\dot{\gamma}^{(\beta)}$ and phase transformation $\dot{\gamma}^{(\chi)}$ are conventionally described based on phenomenological nucleation and growth laws considering stacking fault extension (Wong et al., 2016). The use of phenomenological laws in the CP formulations often introduces excessive parameters, which not only require the validation of the uniqueness of the parameter combinations (Zhang et al., 2022b) but also makes it challenging to precisely quantify the individual contributions of key physical factors (Ding et al., 2019). Therefore, we propose a constitutive law for deformation twinning and phase transformation based on a combination of mechanical and thermal activation events (Dunne et al., 2007). This approach draws parallels with the well-established crystal plasticity formulation based on dislocation slip for FCC alloys, such as Nickel-based superalloys (Bergsmo et al., 2022), the latter of which is given by:

$$\dot{\gamma}^{(\alpha)} = \rho_m b^2 \nu_D \exp\left(-\frac{\Delta F_{ds}}{kT}\right) \sinh\left(\frac{\Delta V_{ds}}{kT} \left|\tau - \tau_c^{(\alpha)}\right|\right), \tag{5}$$

where ρ_m is the mobile dislocation density, b the Burgers vector magnitude, ν_D the dislocation interacting frequency with obstacles, ΔF_{ds} and ΔV_{ds} the activation energy and the activation volume, respectively, k the Boltzmann constant, T the temperature and τ the resolved shear stress. The *sinh*() term incorporates both the forward and backward jumps of dislocations over obstacles, and hence enables the capture of the stress-dependent term at both high and low loading rates (Zhang and Dunne, 2017). The critical resolved

shear stress $\tau_c^{(\alpha)}$ hardens with the dislocation density based on a length-scale-dependent Taylor hardening law:

$$\tau_c^{(\alpha)} = \tau_{c0} + \mu b\sqrt{\rho_{ssd}^{(\alpha)} + \rho_{gnd}^{(\alpha)}}, \tag{6}$$

where τ_{c0} is the intrinsic critical resolved shear stress, μ the shear modulus, and ρ_{ssd} and ρ_{gnd} are the densities of statistically stored dislocations (SSD) and GND, respectively. The evolution of SSD density is correlated to the instantaneous effective plastic strain rate $\dot{p}$ and accumulated plastic strain p (Mecking and Kocks, 1981), where the recovery terms consider the shear resistance saturation when large deformation is present (Lu et al., 2019; Zepeda-Ruiz et al., 2017):

$$\dot{\rho}_{ssd} = \lambda_1 \dot{p} - \lambda_2 p, \tag{7}$$

where λ_1 and λ_2 serve as parameters controlling the slip system hardening and recovery rates, respectively. The effective plastic strain p is given by:

$$p = \sqrt{\frac{2}{3}\boldsymbol{\varepsilon}^{\boldsymbol{p}} : \boldsymbol{\varepsilon}^{\boldsymbol{p}}}, \tag{8}$$

where $\boldsymbol{\varepsilon^p}$ is the plastic strain tensor calculated as the symmetry part of $\boldsymbol{L_p}$.

The GND density ρ_{gnd} in Eq. (6) is calculated from the plastic strain gradients (Arsenlis and Parks, 1999), and a non-local algorithm could relieve the grid size sensitivity of GND density computation (Xu, 2021) over a range of element types. Details about the GND density establishment can be found in (Xu et al., 2021a). It is worth noting that the Bauschinger effect, observed during cyclic loading, arises from the back stresses generated due to the presence of GNDs resulting from the local plastic strain gradient.

In general, deformation twinning and partial dislocations can be interrelated. For example, during the deformation of FCC material, a partial dislocation can nucleate and propagate along a particular slip plane and generate a stacking fault, which can serve as a nucleation site for twinning. A twin boundary can form from the stacking fault, leading to the creation of a twin. Hence, partial dislocations play a crucial role in the formation of deformation twinning. In this work, a stress-driven, thermally activated shear rate of deformation twinning is proposed and written as:

$$\dot{\gamma}^{(\beta)} = \rho_m^{(\beta)} b_p^2 \nu_D \exp\left(-\frac{\Delta F_{tw}}{kT}\right) \sinh\left(\frac{\tau_{eff}^{(\beta)}}{kT}\Delta V_{tw}\right), \tag{9}$$

where $\rho_m^{(\beta)}$ is the mobile dislocation density along the βth twinning system, $b_p = b/\sqrt{3}$ is the Burgers vector magnitude of partial dislocation, and $\tau_{\mathrm{eff}}^{(\beta)} = \tau^{(\beta)} - \tau_{\mathrm{ctw}}^{(\beta)}$ the effective resolved shear stress. It is worth noting that the shear rate is considered as a thermally activated process (Cheng and Ghosh, 2017; Warner et al., 2007) while the nucleation of deformation twinning is temperature-independent and stress-driven (Wagner and Laplanche, 2023) for the Cantor MPEA.

The martensitic transformation from FCC to HCP is generally driven by temperature changes and/or mechanical loading. In this phase transformation, stacking faults and dislocations can play a significant role (Zhang et al., 2017). The martensitic transformation typically begins with the nucleation of small regions of the martensitic phase within the parent phase (FCC). These regions are referred to as martensitic nuclei. Dislocations introduce local lattice distortions and can lower the energy barrier for the nucleation of the martensitic phase, as they, especially partial dislocations or stacking faults, can provide favourable sites for the formation of martensitic nuclei. Once the martensitic nuclei form, the martensitic phase can propagate through the crystal lattice, which involves the glide of dislocations along specific crystallographic planes. Hence, the movement of dislocations is a key mechanism for the growth of martensite domains. Based on these considerations, the shear rate for the martensitic phase transformation from FCC to HCP can be written as:

$$\dot{\gamma}^{(\chi)} = \rho_m^{(\chi)} b_p^2 \nu_D \exp\left(-\frac{\Delta F_{tr}}{kT}\right) \sinh\left(\frac{\tau_{eff}^{(\chi)}}{kT}\Delta V_{tr}\right). \tag{10}$$

It should be noted that in general phase transformation events (e.g. from FCC to BCC structure), hydrostatic pressure could influence the phase transformation process (Tracy et al., 2017) and induce intrinsic strain due to volume changes (Galindo-Nava, 2017). Therefore, when expanding the current phase transformation framework to more general scenarios, it becomes necessary to incorporate the contribution of normal stresses in addition to the shear stresses considered herein, and account for the resulting intrinsic strain. In the present work, we ignore the pressure effect as the volume remains invariant during the FCC to HCP transformation.

It is noted that the shear strain rates induced by dislocation slip, deformation twinning and phase transformation are all described by the unified thermal-activation equations as presented in Eqs. (8)-(10). The coherence of these constitutive equations stems from the commonality that thermal activation events govern the nucleation and propagation of dislocations (Dunne et al., 2007). This unity allows for investigation of the temperature effect on the deformation and damage of MPEAs using the unified constitutive laws. Nevertheless, despite the use of the unified constitutive law, distinctions among the three deformation mechanisms exist, e.g., full dislocations in slip while partial Shockley dislocations in deformation twinning and martensitic phase transformation (Wong et al., 2016), as well as the parameters that control the shear strain evolution, which can vary according to alloy systems.

The evolution rates of volume fraction for deformation twinning and phase transformation are proportional to their respective

shear rate as:

$$\dot{f}^{(\beta)} = \frac{\dot{\gamma}^{(\beta)}}{\gamma_{tw}}, \dot{f}^{(\chi)} = \frac{\dot{\gamma}^{(\chi)}}{\gamma_{tr}}, \tag{11}$$

where $\gamma_{tw} = \gamma_{tr} = \sqrt{2}/2$ are the characteristic shear strains for deformation and martensitic phase transformation in FCC crystals (Lu et al., 2020b). It is noted that the constitutive laws for the three deformation mechanisms could be either rate-sensitive or rate-insensitive, which is related to the material-dependent activation energy and volume (Zhang and Dunne, 2017).

The relative contribution from the three deformation mechanisms is evaluated, respectively, by the ratio of their shear fraction over the total:

$$\begin{aligned}
\phi^{(\alpha)} &= \frac{\sum_{\alpha=1}^{N_{ds}} \gamma^{(\alpha)}}{\sum_{\alpha=1}^{N_{ds}} \gamma^{(\alpha)} + \sum_{\beta=1}^{N_{tw}} \gamma^{(\beta)} + \sum_{\chi=1}^{N_{tr}} \gamma^{(\chi)}}, \\
\phi^{(\beta)} &= \frac{\sum_{\beta=1}^{N_{tw}} \gamma^{(\beta)}}{\sum_{\alpha=1}^{N_{ds}} \gamma^{(\alpha)} + \sum_{\beta=1}^{N_{tw}} \gamma^{(\beta)} + \sum_{\chi=1}^{N_{tr}} \gamma^{(\chi)}}, \\
\phi^{(\chi)} &= \frac{\sum_{\chi=1}^{N_{tr}} \gamma^{(\chi)}}{\sum_{\alpha=1}^{N_{ds}} \gamma^{(\alpha)} + \sum_{\beta=1}^{N_{tw}} \gamma^{(\beta)} + \sum_{\chi=1}^{N_{tr}} \gamma^{(\chi)}},
\end{aligned} \tag{12}$$

where $\phi^{(\alpha)}$, $\phi^{(\beta)}$ and $\phi^{(\chi)}$ are the volume fraction for dislocation slip, deformation twinning and phase transformation, respectively.

These newly proposed constitutive laws for twinning and phase transformation unify the shear rate computation for all three deformation mechanisms, and hence enables a systematic investigation of the temperature-governing behavior of MPEAs through a relatively small number of well-defined parameters. The specific material properties for single-phase, equiaxed Cantor alloy MPEA are discussed and provided in Section 3.

2.1.2. *Short-range order in the crystal plasticity framework*

The influence of SRO on the mechanical behaviour of grains (Bu and Wang, 2021; Cao et al., 2020; Chen et al., 2022; Li et al., 2023) can be incorporated into the multi-mechanism CP framework by considering the local variations in mechanical properties, such as modulus, slip strength, activation energy etc., at finite element integration points. Given the complexity of SRO effect, the present study confines the overall SRO effect to a statistical distribution of intrinsic slip strength τ_{c0} (as seen in Eq. (6)) with a mean value $\overline{\tau}_{c0}$ and a standard deviation over a specified length scale. The mean value and standard deviation, which represents the homogeneous part

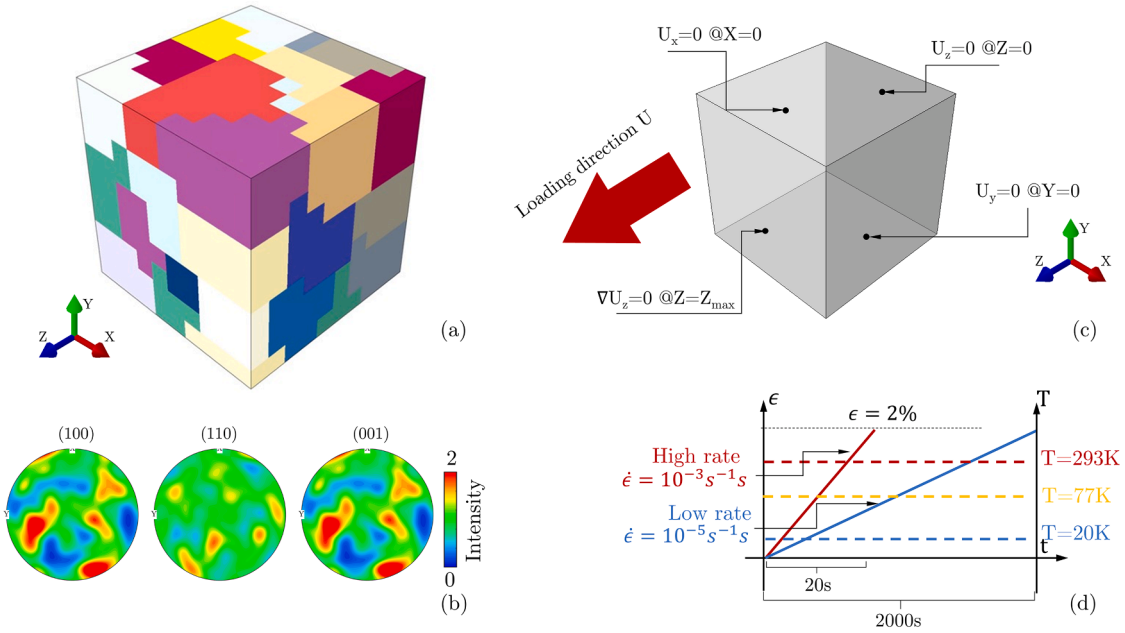

Fig. 1. The full three-dimensional representative volume element (RVE) model for validating the proposed CPFE framework and calibrating the temperature-dependent material properties of CrMNFeCoNi MPEA. (a) The microstructure of the polycrystalline cubic RVE and crystals with different orientations are coloured differently. (b) The pole figures of the RVE showing a weak texture. (c) Schematic showing the boundary conditions and uniaxial loading imposed on the RVE. (d) The two loading rates and two ambient temperatures applied to the RVE. (For interpretation of the references to colour in this figure legend, the reader is referred to the web version of this article.)

(non-SRO affected) and the local fluctuation part (SRO affected) of the slip strength, respectively, are determined by calibrating the macroscopic response and the results are detailed in Section 3.1 below. In the calibration, a specified length scale of 25 μm was selected and the details of the calculation can be found in Fig. A3. The selection of the length scale is to reflect on the experimental characterization (Li et al., 2019a) of dislocation line movement velocity (v_{dis}=25 m•s^{-1}) within a typical CP time increment ($\Delta t=10^{-6}$ s). It is worth noting that this estimated length scale is comparable with the representative grain sizes observed in both the Cantor alloy (Gludovatz et al., 2014; Li et al., 2022b) and the CrCoNi MEA (Liu et al., 2022) after heat treatment.

2.2. Representative volume element model and parameters identification

A full three-dimensional representative volume element (RVE) CPFE model is developed to validate the newly proposed SRO-enhanced multi-mechanism CPFE framework and to calibrate material properties against experimental measurements. The polycrystalline finite element model adopted herein contains 50 grains, as illustrated in Fig. 1(a). The various colours in the figure represent different crystallographic orientations within the microstructure. The investigated CrMnFeCoNi MPEA normally has a weak texture (Gludovatz et al., 2014; Kumar et al., 2023; Liu et al., 2022) such that a random set of grain crystallographic orientations are assigned to the grains, as depicted in the pole figures shown in Fig. 1(b). The RVE is discretized into 10 × 10 × 10 C3D8R elements, which are hexagonal-shaped reduced integration continuum elements. This element arrangement ensures that the mesh size is sufficiently fine to diminish grid size sensitivity (Lu et al., 2020b; Zhang et al., 2022b), and the mesh sensitivity study is shown in Fig. A2. Boundary conditions are applied to the RVE, as illustrated in Fig. 1(c), to simulate both strain-controlled uniaxial tension loading and a generalized plane strain scenario. Specifically, the left, bottom and back faces of the RVE are constrained along the X-, Y- and Z-directions, respectively. Displacement is imposed onto the front face (i.e. $Z=Z_{Max}$) along the Z-direction. Two typical loading rates are realized by applying the desired maximum strain level (2%) within the corresponding loading period, and two typical ambient temperatures (namely room temperature 293 K and liquid nitrogen temperature 77 K) are set up (Fig. 1(d)), respectively, to extract the parameters governing strain-rate sensitivity and temperature sensitivity of the CrMnFeCoNi MPEA RVE model.

Another quasi-3D RVE model is developed to understand the cyclic behaviour of CrMnFeCoNi MPEA at the following three temperatures, 293 K, 77 K and 20 K. The quasi-3D RVE contains 100 single-phased equiaxed FCC grains with an average grain size of $\bar{d}$=21 μm, and the crystallographic orientations of the 100 grains follow a random distribution. The microstructure of the RVE model, as depicted in Fig. 2, more accurately represents the essential microstructure features observed in the specimen in independent tests (Gludovatz et al., 2014; Liu et al., 2022), which are summarized in Fig. 2(a) and (b). The fact that the grain orientations remain unchanged throughout the thickness aligns with the experimental observations of the thin cross-sectioning (Liu et al., 2022). A plane strain boundary condition is applied to the RVE (sketched in Fig. 2(c)) for simulating the response of the material near the mid-section plane. The RVE is discretised into 20,000 C3D20R finite elements (i.e. the 2nd order, hexagonal-shaped, reduced integration continuum element). The loading is realized through imposing a displacement along the right-hand-side face (i.e. $X=X_{Max}$) of the RVE. The displacement follows a low cycle fatigue (LCF) profile with a period of 4000 s, and five consecutive cycles are simulated at the following three isothermal temperatures: 293 K, 77 K and 20 K. The loading and temperature histories for the cyclic loading are schematically shown in Fig. 2(d).

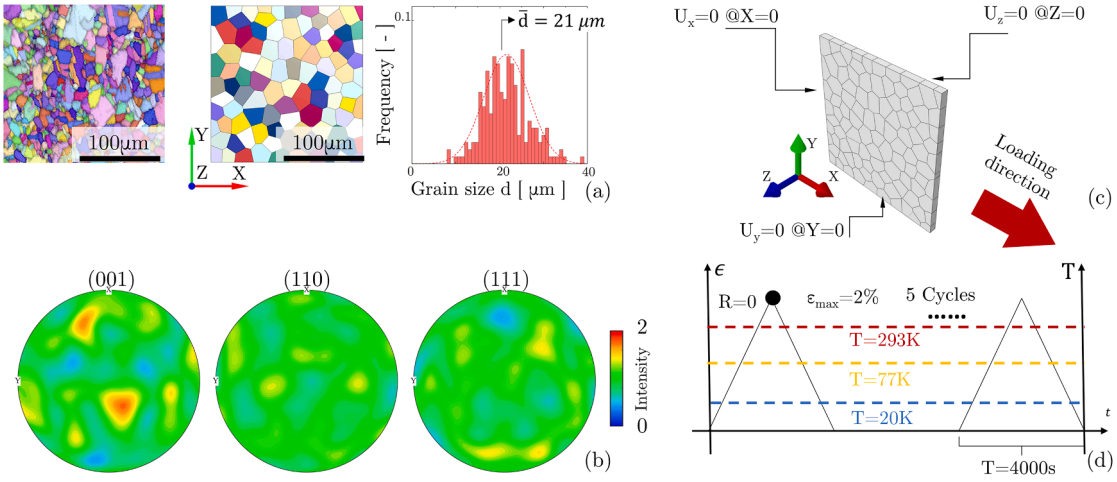

Fig. 2. The quasi three-dimensional Representative Volume Element (RVE) model for understanding the cyclic behaviour of CrMnFeCoNi MPEA under three typical temperatures. (a) The microstructure information of the RVE model with comparison to the experimental characterization (Gludovatz et al., 2014; Liu et al., 2022). (b) The pole figures of the RVE showing a weak texture. (c) Schematic illustration of the boundary conditions and strain-controlled loadings imposed on the RVE. (d) The cyclic loading history and three ambient temperatures applied.

2.3. Mechanistic driver for crack nucleation

In this study, stored energy density (SED) is employed to assess the fatigue damage and crack nucleation of the CrMnFeCoNi MPEA under cyclic loading. SED serves as a micro-mechanical metric that takes into account the damage resulting from dislocation slip and interaction within a local dislocation structure where dislocation-associated energy is stored (Xu et al., 2021b). It quantifies the energy required for the initiation of two crack surfaces, akin to the Griffith criterion.

The stored energy density G is defined as:

$$G = \int \frac{\xi \boldsymbol{\sigma} : d\boldsymbol{\varepsilon}^{\mathrm{p}}}{\sqrt{\rho_{ssd} + \rho_{gnd}}}, \tag{13}$$

where ξ is the fraction of plastic work stored in a dislocation structure and estimated as 0.05 (Kamlah and Haupt, 1997). SED has been shown to be a faithful microstructure-sensitive measure to predict the potential crack nucleation sites (Wan et al., 2023) and the short crack propagation in different ductile alloys (Long and Dunne, 2023).

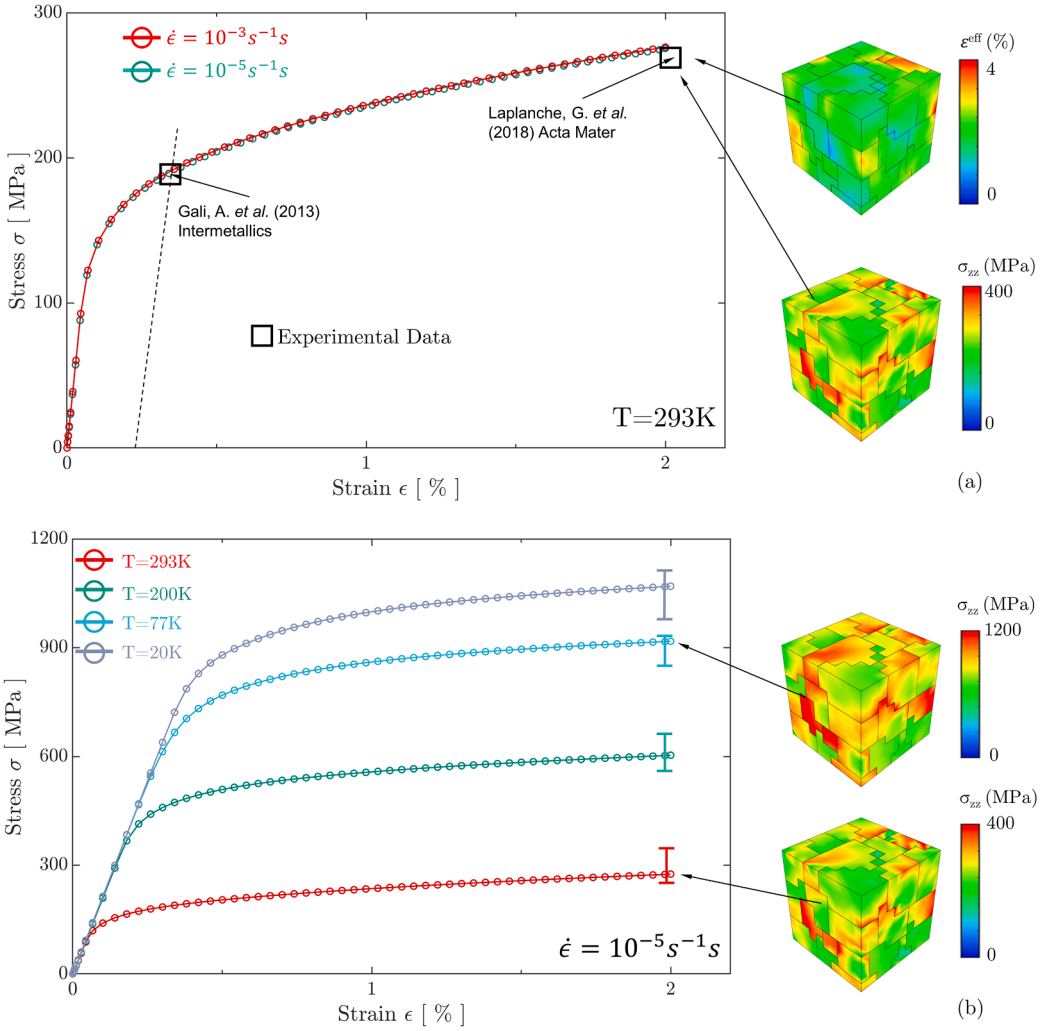

Fig. 3. The monotonic uni-axial tension stress-strain response of the three-dimensional cubic RVE subject to (a) two different loading rates at room temperature and (b) four temperatures at the loading rate $\dot{\epsilon} = 10^{-5}s^{-1}$. The black dashline indicates the 0.2% yield stress, and the experimental data was gleaned from a tensile test with strain rates as $\dot{\epsilon} = 10^{-5}s^{-1}$ and $\dot{\epsilon} = 10^{-3}s^{-1}$ at room temperture.

3. Results and discussion

3.1. Temperature-dependent mechanical behaviours

The identification of material parameters and the resulting stress-strain curves of the polycrystal CrMnFeCoNi MPEA RVE (depicted in Fig. 1) subject to different loading rates and temperatures are shown in Fig. 3. The fundamental mechanical properties, including moduli (Laplanche et al., 2015), critical resolved stress (Kawamura et al., 2021; Laplanche et al., 2016; Otto et al., 2013), activation energy and activation volume (Laplanche et al., 2018; Xie et al., 2020) and their dependence on temperature are obtained from literature, while the hardening related parameters are calibrated against experimental data (Gali and George, 2013). Fig. 3(a) shows the stress-strain response of the RVE subject to two distinct strain rates $\dot{\epsilon} = 10^{-5}s^{-1}$ and $\dot{\epsilon} = 10^{-3}s^{-1}$ at room temperature, 293 K. The strain-rate sensitivity (SRS) at room temperature is shown to be extremely low for CrMnFeCoNi as the stress discrepancy is limited. The reason for the low SRS is consistent with experimental analysis (Laplanche et al., 2018), and is mechanistically rationalized by the large value of activation volume at room temperature in the CPFE model (see the discussion in (Zhang and Dunne, 2017)). The temperature-dependent stress-strain curves at four typical temperatures, 293 K, 200 K, 77 K and 20 K, are reported in Fig. 3(b) subject to the low strain rate. The model captures the stress level at 2% and its dependence on temperatures ranging from 20 K to 293 K with comparison to experimental data (Gali and George, 2013; Gludovatz et al., 2014; Ming et al., 2020; Naeem et al., 2020), which scatter due to different grain sizes, heat treatment and loading conditions. The model predicts a much-strengthened stress response of CrMnFeCoNi MPEA at low temperatures. The discussion of deformation mechanisms, as well as the contributions arising from the increased elastic modulus, shear modulus and the critical resolved shear stress for dislocation slip at low temperatures, will be presented in more details in the following section (see Table 1). The temperature-dependent material properties of CrMnFeCoNi MPEA for the CPFE modelling are tabulated in Table 1. Low-scale calculations such as Discrete Dislocation Dynamics (Fang et al., 2022) and Molecular Dynamics (Rao et al., 2017) could potentially be adopted in the future to provide more physics-based approaches to determine parameters in the current multi-mechanism framework.

The temperature-dependence of the individual deformation mechanisms, dislocation slip, deformation twinning and phase transformation, with applied strain are reported in Fig. 4 in terms of dislocation density, volume fraction of twinning and martensitic phase transformation at the three investigated temperatures (293 K, 77 K and 20 K). Dislocation slip is observed in the RVE at all three temperatures, and the dislocation density increases with temperature due to the thermal activation effect. Deformation twinning is seen at 77 K and 20 K as the strain level at 2% but not at 293 K (Laplanche et al., 2016). Martensitic phase transformation is predicted to take place at 20 K only, and the amount of the phase transformation is quite limited (less than 2% as the volume fraction averaged all through RVE). The temperature-dependence of the individual deformation mechanisms is well consistent with experimental findings (Tirunilai et al., 2020). The activation sequence of the deformation mechanisms is shown to be dislocation slip, followed by deformation twinning and martensitic phase transformation at 20 K, which are associated with their CRSS values. The monotonic tensile results validate the temperature-sensitivity of individual deformation mechanisms in CrMnFeCoNi MPEA, thereby providing the basis for investigating the cyclic behaviour at different temperatures, which will be discussed in the following sections.

The effect of SRO on the mechanical behaviour of CrMnFeCoNi MPEA is investigated via the uniaxial tension case at room temperature (293 K) and a low loading rate ($10^{-5}s^{-1}$). The incorporation of the SRO effect into the multi-mechanism CPFE framework is illustrated in Fig. 5(a). In cases with SRO, material points exhibit an intrinsic slip strength characterized by a Gaussian distribution, in contrast to a constant value in those without SRO. The mean value of this distribution is chosen to match that extracted from corresponding tensile experiments (tabulated in Table 1). Meanwhile, the standard deviation is calibrated against independent experimental results (Gali and George, 2013), particularly when the strain is large enough to show apparent plastic strain. The stress versus strain response is shown in Fig. 5(b) for the RVE with and without the SRO effect. In this case, the standard deviation of the slip strength, set at 18% of the mean value, effectively captures the observed increase in yield stress due to SRO, as reported in experiments (Zhang et al., 2020). The introduction of statistical intrinsic slip strength results in additional deformation heterogeneity, alongside the

Table 1
Temperature-dependent material properties for CrMnFeCoNi MPEA polycrystal samples (valid from 20K-293 K). The temperature T is given in Kelvin.

Symbol	Physics description	Value
E	Elastic modulus	$214 - 35/(\exp(416/T - 1))$ GPa
μ	Shear modulus	$85 - 16/(\exp(448/T - 1))$ GPa
τ_{c0}	Critical resolved shear stress for dislocation slip	$169\exp(-0.0048T)$ MPa
τ_{ctw}	Critical resolved shear stress for twinning	235 MPa
τ_{ctr}	Critical resolved shear stress for phase transformation	405 MPa
λ_1	Hardening coefficients	300 μm^{-2}
λ_2		5 μm^{-2}
ρ_{ini}	Initial dislocation density	0.1 $\mu m^{-2}s^{-1}$
k	Boltzmann constant	1.38×10^{-23} J•K^{-1}
ΔF	Activation energy*	280 kJ•mol^{-1}
ΔV	Activation volume*	$37.95\exp(0.0071T)$ b^3

* The activation energy and volume for dislocation slip, deformation twinning and phase transformation are considered to be identical as the corresponding apparent values that were measured in the macroscopic experimental tests (Laplanche et al., 2018; Xie et al., 2020).

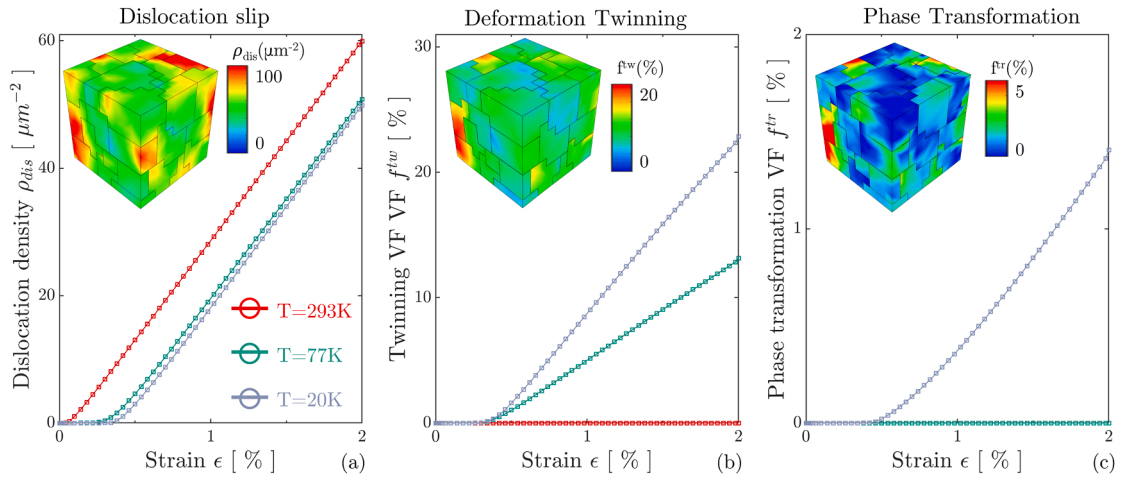

Fig. 4. Overall evolution of the (a) dislocation density, (b) volume fraction of deformation twinning and (c) volume fraction of phase transformation within the cubic RVE under the three investigated temperatures subject to the loading rate $\dot{\epsilon} = 10^{-5}s^{-1}$ of uniaxial tension.

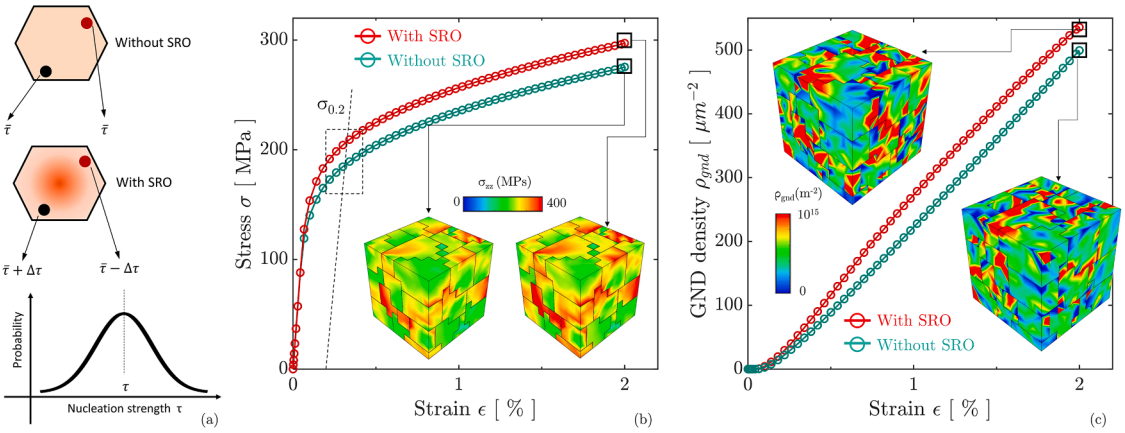

Fig. 5. The short-range order (SRO) effect on the response of the cubic RVE at room temperature and loading rate $\dot{\epsilon} = 10^{-5}s^{-1}$. (a) A schematic illustration of the SRO effect on the nucleation strength of dislocations along slip systems. (b) The stress strain responses of the cubic RVE with and without considering the SRO effect. (c) The geometrically necessary dislocation (GND) development in the RVE with and without considering the SRO effect.

crystallographic orientation, grain size and grain boundary morphology within the polycrystal RVE. This added heterogeneity leads to the generation of GNDs due to the presence of additional strain gradient. The overall GND density, which represents the average density throughout the RVE model, is compared in Fig. 5(b) for the cases with and without SRO. In the case with SRO, there is a 9% higher GND density, attributed to the heterogeneity introduced by the local fluctuations in deformation. Therefore, we propose that the enhancement in the yield stress (Antillon et al., 2020; Zhang et al., 2022a) and micro-hardness (Wu, 2023) in the MPEAs can be attributed to the formation of additional GNDs through SRO-induced local variations in mechanical properties. The difference in GND density as shown in Fig. 5(c) is not substantial, given that the polycrystal RVE itself contains grain-scale inhomogeneity such as crystallographic orientation and grain size. Hence, in the following, a single crystal case is adopted to decouple the fundamental grain-scale inhomogeneity from the model to further investigate the SRO effect. The macroscopic stress response does not show stochastic features, unlike those modelled using discrete dislocation dynamics (Xu et al., 2023). This absence of stochastic behaviour can be attributed to the large number of elements and the small fraction of standard deviations obtained here.

The SRO effect is investigated in a single crystal that has no grain-scale inhomogeneity at room temperature. The single crystal CrMnFeCoNi MPEA is loaded in tension along its [001] orientation. A comparison of the stress vs. strain response, as depicted in Fig. 6 (a), reveals an enhancement in the yield stress due to the presence of SRO, despite the mean values of the intrinsic slip strength being identical for both cases, with and without SRO. The inset in Fig. 6(a) displays the GND distribution at 2% strain, where the single crystal with SRO exhibits a significant GND density, while the one without SRO shows no GND through the grain and the deformation remains completely homogenous. Fig. 6(b) shows the statistical distribution of plastic strain within the single crystals with and without SRO. In contrast to one single value observed in the case without SRO, the case with SRO shows a much wider distribution of plastic

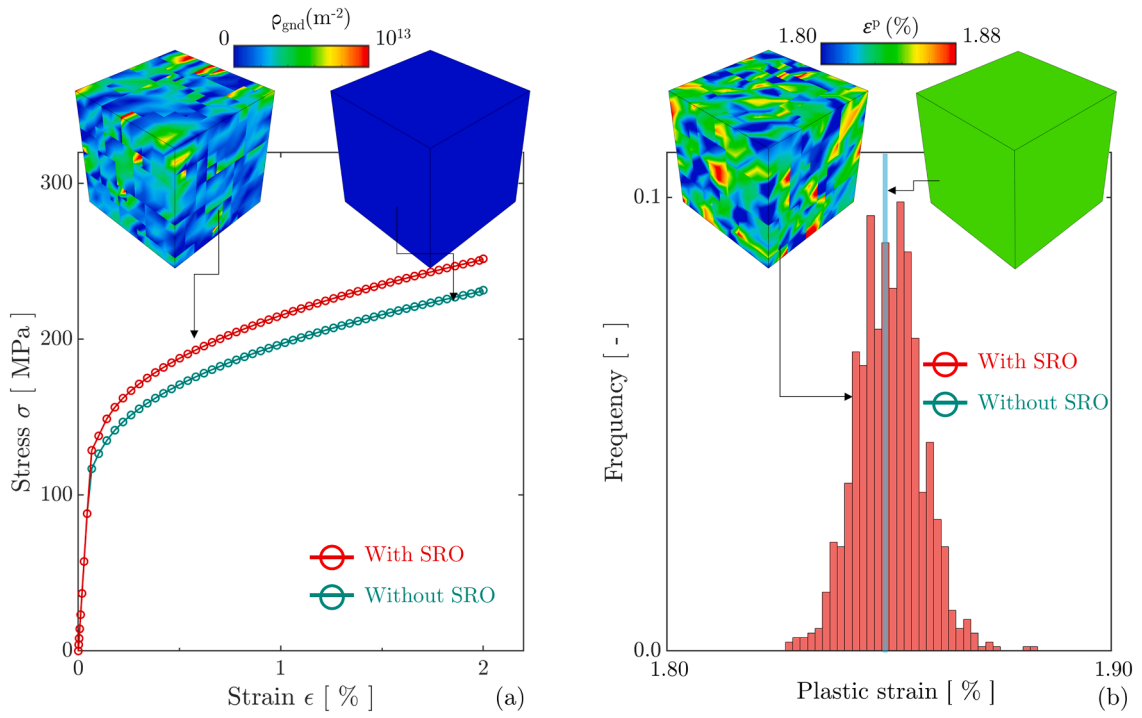

Fig. 6. The SRO effect on the response of a single crystal ((001) with respect to the loading direction) at room temperature. (a) The stress strain responses of a single crystal with and without considering SRO effect. (b) The plastic strain developed in the single crystal with and without considering SRO effect.

strain due to local inhomogeneity. This distribution closely resembles the Gaussian distribution observed in direct measurements of local strain distribution in a similar MPEA (Chen et al., 2021b). The notable difference in GND density observed in the single crystal cases clearly demonstrates the impact of the SRO effect through inhomogeneity and associated enhancement of yield stress in MPEA. This finding sheds light on the underlying mechanism responsible for the increase in yield strength observed in MPEAs and offers a mechanistic explanation for the experimental observation that deformation twinning activities are enhanced (Jian et al., 2020; Li et al., 2022b) when SRO is stronger, which could be attributed to the rise of local stresses induced by SRO.

3.2. *Cyclic behaviours under three typical temperatures*

The evolution of effective plastic strain, stress and stored energy density (SED) within the RVE (see Fig. 2) that reflects a realistic microstructure of CrMnFeCoNi MPEA polycrystal sample is shown in Fig. 7 at four instants, namely half-load, peak load, half-unload and fully unload, during the 1^{st} cycle at 293 K. The direct stress (2nd row) achieves a maximum at the peak load instant, and residual stresses are developed at the unload instant due to back stress and GND effect (Lu et al., 2020b). As the plastic strain accumulates progressively during the whole cycle, a large portion (~10%) of residual plastic strain becomes highly localized (indicated by the black-framed circle) due to the microstructural inhomogeneity. As a consequence of both the residual stress and plastic strain, SED is also localized within this region; recall the definition of SED in Eq. (13).

The cyclic behaviour of plastic strain, stress and SED of the RVE is recorded at the peak load instant during each loading cycle and reported in Fig. 8 for the initial five cycles. With each cycle, both the plastic strain and stress show a progressive increase, which reflects the synergistic feature of strength and elongation of CrMnFeCoNi MPEA (Zhang et al., 2014). However, compared to the instantaneous plastic strain and stress distributions, the SED accumulation exhibits a more localized feature, and the location is indicated by the circled area, where a fatigue crack would eventually nucleate as a result of the build-up of SED, causing the opening of two micro-facets (Chen et al., 2018). The underlying mechanisms for the localization of plastic strain, stress and SED will be detailed in the following figure and discussion. The stress levels experienced during the 1^{st} to 5^{th} cycles are still not high enough to activate deformation twinning or phase transformation, which is consistent with experimental findings (Gludovatz et al., 2014).

The localization of the cyclic SED developed at room temperature within the RVE is analysed in Fig. 9 at the peak load instant of the 5^{th} cycle. A close-up view of the effective plastic strain distribution within the region, where the SED is highly localized in the whole RVE (see Fig. 9(a)), is shown in Fig. 9(b), and a large portion of plastic strain (up to 30%) is seen near the grain boundaries and triple junctions among grains G2-G6 (labelled in Fig. 9(b)), while the strain level at the grain boundary between G7 and G8 is relatively low. The GND distribution along with the activated slip planes (indicated with white dashed lines) is plotted in Fig. 9(c) for the investigated set of grains. Multiple slip systems are activated within G2-G6, resulting in an increase in the GND density (Cao, 2022; Lu et al., 2020a).

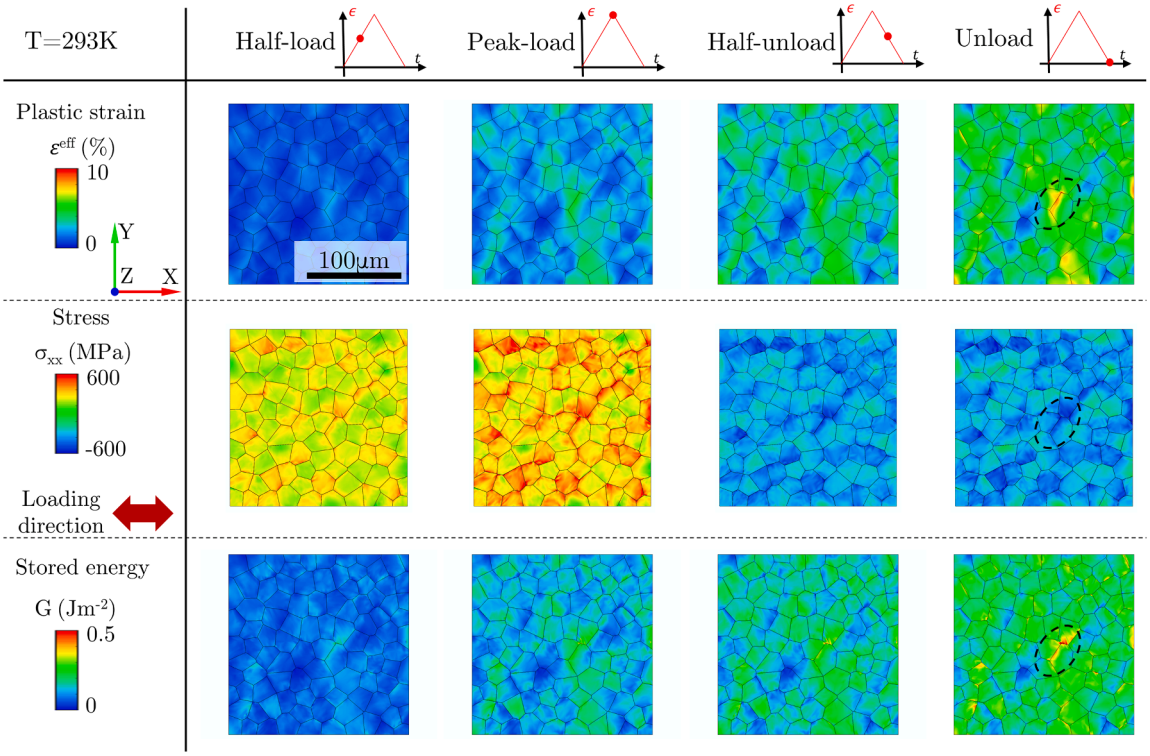

Fig. 7. The evolution of plastic strain, stress and stored energy density (SED) in the quasi 3D RVE during the 1st cycle of a $R = 0$ cyclic loading at room temperature (293 K). The volume fractions of deformation twinning and phase transformation remain zero. (For interpretation of the references to colour in this figure legend, the reader is referred to the web version of this article.)

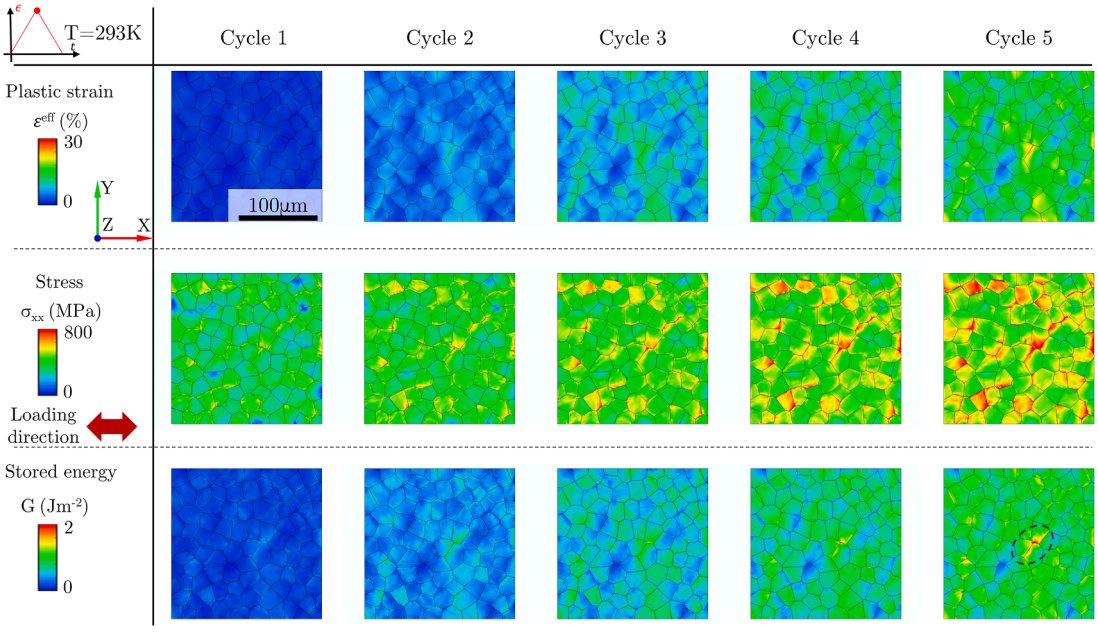

Fig. 8. The cyclic evolution of plastic strain, stress and stored energy density (SED) in the quasi 3D RVE for the first 5 cycles at room temperature. The volume fractions of twinning and phase transformation remain zero for the cycles investigated here. (For interpretation of the references to colour in this figure legend, the reader is referred to the web version of this article.)

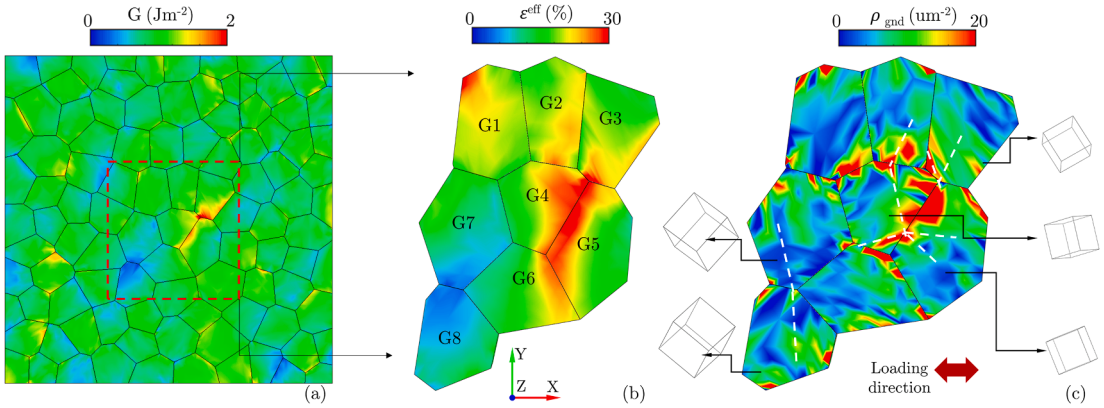

Fig. 9. (a) The localization of SED within the RVE at the peak load instant of the 5th cycle, which is caused by the strong strain gradient nearby (b) and the multi-slip system activation with GND distribution (c). The strong localization of SED could eventually lead to fatigue crack nucleation. The unit cells in (c) illustrate the crystallographic orientations of the specific grains.

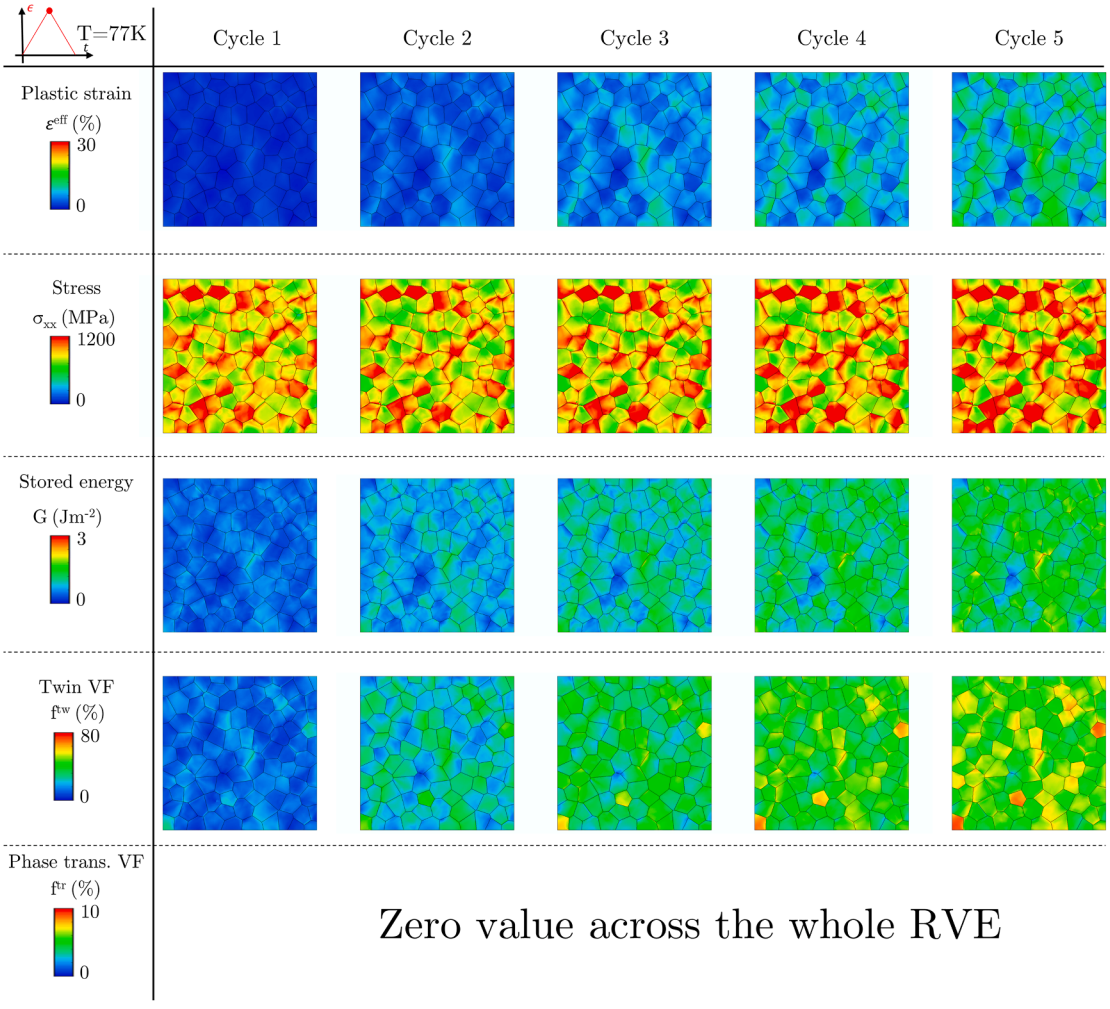

Fig. 10. The cyclic evolution of plastic strain, stress, stored energy density (SED) and the volume fraction of deformation twinning within the quasi 3D RVE for the first 5 cycles at 77 K. The volume fraction of martensitic phase transformation remains zero for the cycles investigated here. (For interpretation of the references to colour in this figure legend, the reader is referred to the web version of this article.)

This leads to highly localized strain and SED as shown in Fig. 9(a) and (b), which could potentially result in local damage and fatigue crack nucleation (Suresh, 2012). The unit cells in Fig. 9(c) visually highlight the large difference in crystallographic orientations of some of the grains, which leads to the activation of multiple slip systems to accommodate the inhomogeneity. In contrast, the grain orientations of G7 and G8 are similar, resulting in the activation of a single slip system. This similarity helps reduce the plastic strain gradient and SED.

The cyclic behaviour of plastic strain, stress, SED and the twinning volume fraction of the RVE at liquid nitrogen temperature (77 K) are recorded at the peak load instant during each loading cycle and shown in Fig. 10 for the first five cycles. It is seen that the plastic strain accumulation slows down and the direct stress achieves a saturated status with cycles. The slowdown of plastic strain accumulation is due to the nucleation and progressive growth of deformation twins, which is represented in terms of its volume fraction in the 4th row of Fig. 10. Therefore, although the stress level is much higher than that at 293 K, the SED (the 3rd row) accumulation rate is not seen to considerably surge, reflecting the influence of the dynamic Hall-Petch effect (De Cooman et al., 2018). In addition, the plastic strain and SED distribution are seen to be more homogenous rather than highly localized at certain regions due to the competitive interaction between dislocation slip and deformation twinning (Woo et al., 2023), which could potentially delay fatigue crack nucleation (Zhang et al., 2015). Therefore, the activation of deformation twinning at 77 K facilitates the damage tolerance of the CrMnFeCoNi MPEA (Lam et al., 2020) through depressing dislocation glide and stored energy localization (Wu and Fan, 2020), which agrees with the experimental observation (Gludovatz et al., 2014, 2016).

The cyclic behaviour of plastic strain, stress, SED, twinning, and the phase formation volume fraction of the RVE at near liquid helium temperature (20 K) are recorded at the peak load instant of each loading cycle and shown in Fig. 11 for the first five cycles. Compared to the results predicted at 77 K (see Fig. 10), a limited but notable amount of martensitic phase transformation is observed. The nucleation and growth of transformed martensite further hardens (Lu et al., 2020b; Niu et al., 2018) CrMnFeCoNi MPEA as the stress continues to increase. The increase in plastic strain and SED during cyclic loading at 20 K, however, is not significant compared to those at 293 K and 77 K. This is due to the additional amount of deformation twinning taking place at 20 K compared to that at 77 K and the addition of martensitic phase transformation. Therefore, the excellent damage resistance of CrMnFeCoNi MPEA at 20 K can be attributed to the slow accumulation of SED over cycles, which is facilitated by the phase transformation along with extra deformation twinning, which also strengthens the stress response. It is worth noting that the volume fraction of martensitic phase transformation under cyclic loading is higher than that under monotonic loading (see Fig. 4(c)).

The temperature-dependent plastic strain, stress and stored energy developed within the RVE are compared in Fig. 12 for the three temperatures at the peak load instant of 5^{th} Cycle. Compared to the case of room temperature 293 K, the effective plastic strain and localization do not exhibit significant increases at 77 K, despite the significant rise in stresses due to continued hardening (Li et al., 2019b). The saturated plastic strain and its distribution (leading to GND distribution through plastic strain gradient) at lower temperatures alleviate the accumulation of SED over cycles. This effect can be attributed to the activation of deformation twinning and limited amount of martensitic phase transformation in CrMnFeCoNi MPEA. Therefore, the CPFE analysis provides a mechanistic understanding for the excellent damage tolerance of CrMnFeCoNi MPEA at low (Gludovatz et al., 2014, 2016) and extremely low temperatures (Liu et al., 2022).

The individual contribution from each deformation mechanism to the overall plastic deformation is shown in Fig. 13(a) at the peak load instant of the 5^{th} cycle at the three investigated temperatures. The contribution is quantified as the average value through the whole RVE using Eq. (12). Dislocation slip carries all plastic deformation at room temperature (293 K) as there is no deformation twinning or phase transformation up to the 5^{th} cycle (see also Fig. 8 above). At 77 K, a considerable amount of deformation twinning is activated, leading to a contribution of 35% to the overall plastic deformation. Deformation twinning becomes even more pronounced at 20 K, accounting for more than 50% of the total plastic deformation, while a limited portion (~4%) of martensitic phase transformation occurs in the RVE at this temperature. The cyclic crystal plasticity analysis reflects the experimental characterization of the sequence of the hardening mechanisms in CrMnFeCoNi MPEA at cryogenic temperatures (Gludovatz et al., 2014; Kawamura et al., 2021; Liu et al., 2022). Hence the present study sheds light on the synergistic relationship between strength and toughness of CrMnFeCoNi MPEA. Specifically, the nucleation and growth of deformation twinning and martensitic phase transformation play a major role in delocalizing the stored energy at lower temperatures. The evolution of the fraction of individual contributions with the number of cycles is reported in Fig. 13(b) at the temperature 20 K. Dislocation slip initially dominates the total plastic strain, but its contribution is overtaken by deformation twinning at the 5^{th} cycle, and the contribution of phase transformation continues to rise within the first 5 cycles. Further investigation on the competition and/or cooperation among the three deformation mechanisms in MPEA has the potential to further enhance the synergy between strength and ductility through microstructure optimization.

4. Conclusions

A temperature-dependent, multi-mechanism crystal plasticity framework which incorporates dislocation slip, deformation twinning and martensitic phase transformation at the grain scale is proposed with a unified constitutive law accounting for all three deformation mechanisms. Comprehensive simulations using representative volume element (RVE) models applied to the Cantor alloy-like MPEAs under both uniaxial tension and cyclic loading conditions were analysed at three typical temperatures. Key findings include:

- The rate- and temperature-sensitivity of the stress-strain response is captured using the material properties calibrated against experimental tests. In addition, the occurrence and sequence of twinning and martensitic phase transformation reflect the deformation mechanisms observed experimentally at lower temperatures;

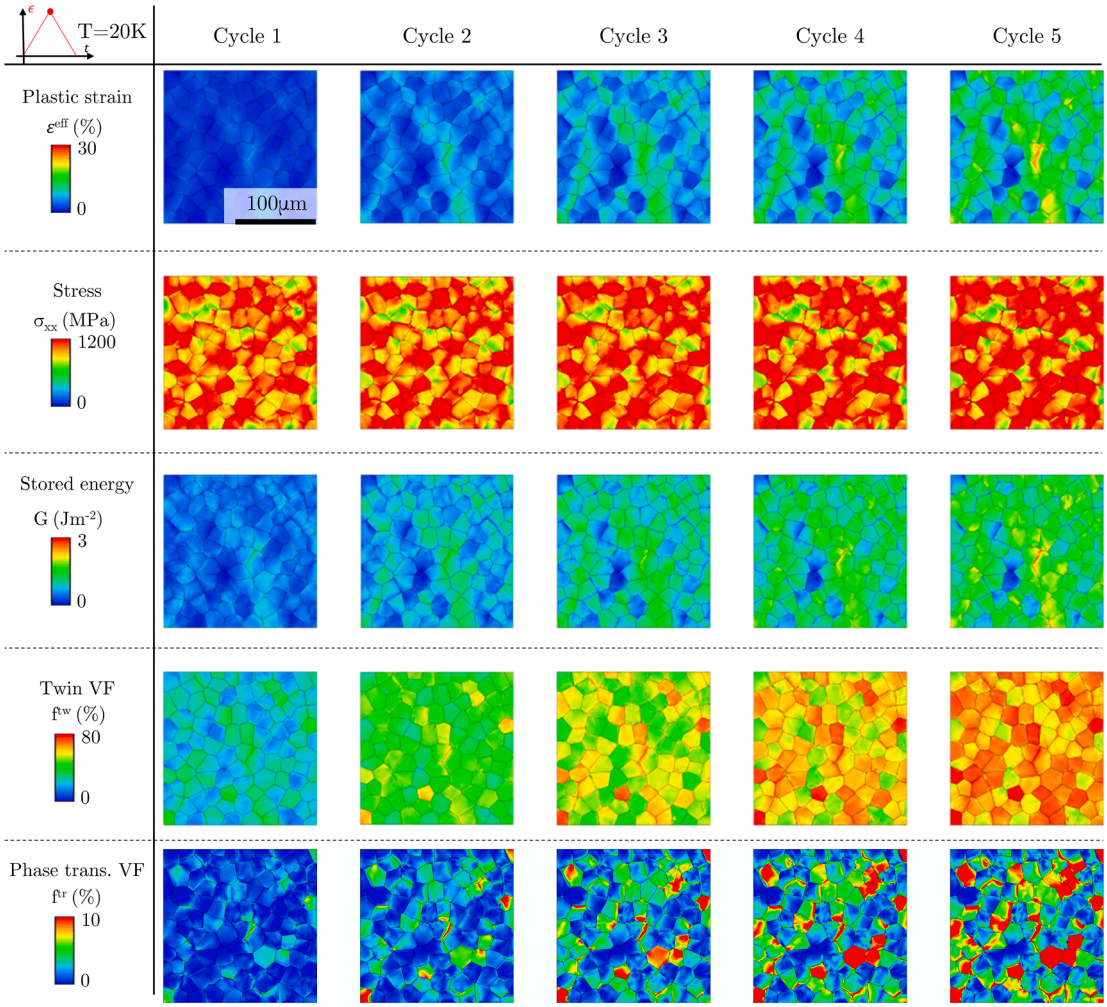

Fig. 11. The cyclic evolution of plastic strain, stress, SED, and the volume fractions of deformaton twinning and martensitic phase transformation within the quasi-3D RVE for the first 5 cycles at 20 K. Significant volume fraction of deformation twinning and notable volume fraction of martensitic phase transformation are predicted. (For interpretation of the references to colour in this figure legend, the reader is referred to the web version of this article.)

- The enhancement of the mechanical response of Cantor alloy-like MPEAs due to the SRO effect has been linked to the generation of GNDs resulting from local material property variations;
- The excellent fatigue and fracture resistance of Cantor alloy-like MPEAs at low temperatures can be attributed to the homogenization of SED within the microstructure. Such homogenization is a result of the development of deformation twinning and martensitic phase transformation, as revealed by the present study.

CRediT authorship contribution statement

Yilun Xu: Conceptualization, Methodology, Software, Writing – original draft, Visualization. **Xiaochong Lu:** Conceptualization, Formal analysis, Investigation, Methodology, Visualization. **Xinyu Yang:** Methodology, Writing – review & editing. **Wanghui Li:** Writing – review & editing. **Zachary Aitken:** Writing – review & editing. **Guglielmo Vastola:** Writing – review & editing. **Huajian Gao:** Conceptualization, Methodology, Writing – review & editing, Supervision. **Yong-Wei Zhang:** Conceptualization, Methodology, Writing – review & editing, Supervision.

Declaration of competing interest

The authors whose names are listed immediately below certify that they have NO affiliations with or involvement in any organization or entity with any financial interest (such as honoraria; educational grants; participation in speakers' bureaus; membership, employment, consultancies, stock ownership, or other equity interest; and expert testimony or patent-licensing arrangements), or non-

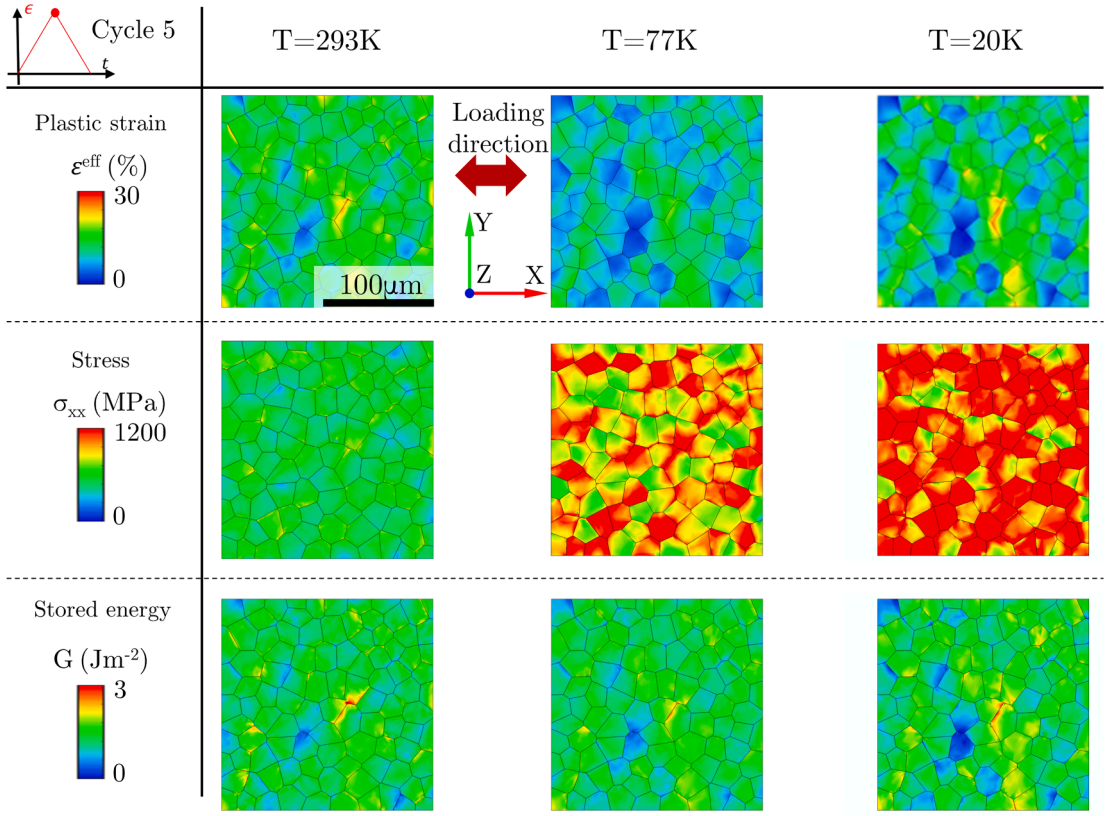

Fig. 12. The comparison of plastic strain, stress and SED developed within the RVE at the peak load instant of the 5th cycle at the three temperatures investigated here.

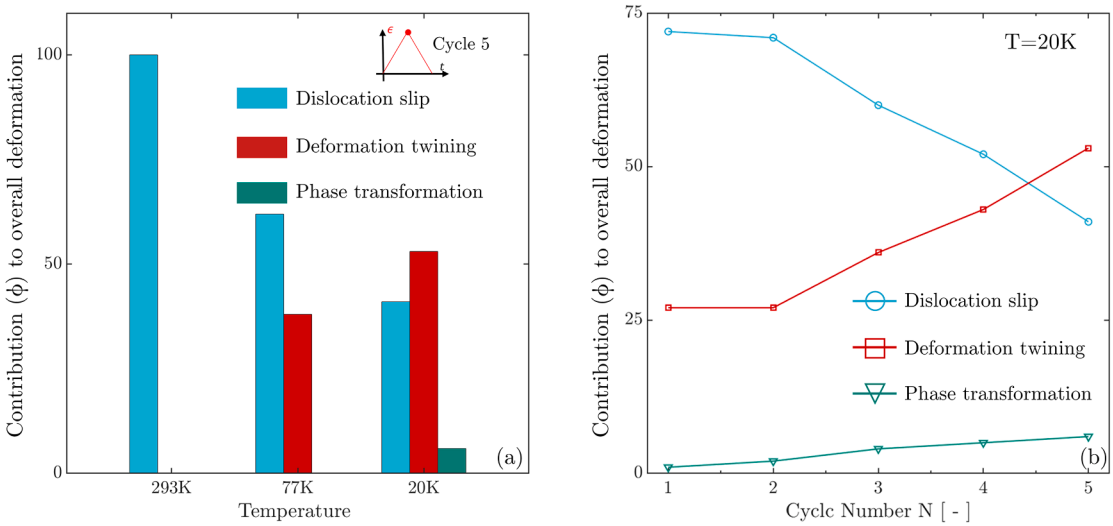

Fig. 13. The contribution of the individual deformation mechanisms of dislocation slip, deformation twinning and phase transformation to the overall plastic deformation of the RVE model. The results are recorded at the peak load instant under the three investigated temperatures at the 5th cycle (a) and with the number of loading cycle at 20 K (b).

financial interest (such as personal or professional relationships, affiliations, knowledge or beliefs) in the subject matter or materials discussed in this manuscript.

Data Availability

Data will be made available on request.

Acknowledgement

YX, GV and YWZ acknowledge the financial support by the Agency for Science, Technology and Research (A*STAR) under grant AMDM A1898b0043 and the MTC Programmatic funding under the grant M22L2b0111. HG acknowledges the MTC Programmatic funding under the grant M22L2b0111. XL acknowledges the financial support by the National Natural Science Foundation of China (Grant No.92263201, 12302280), the Project funded by China Postdoctoral Science Foundation (2022M722253), and the Postdoctoral joint training program of Sichuan University (SCDXLHPY2308).

Appendix

Fig. A1, A2, A3, A4

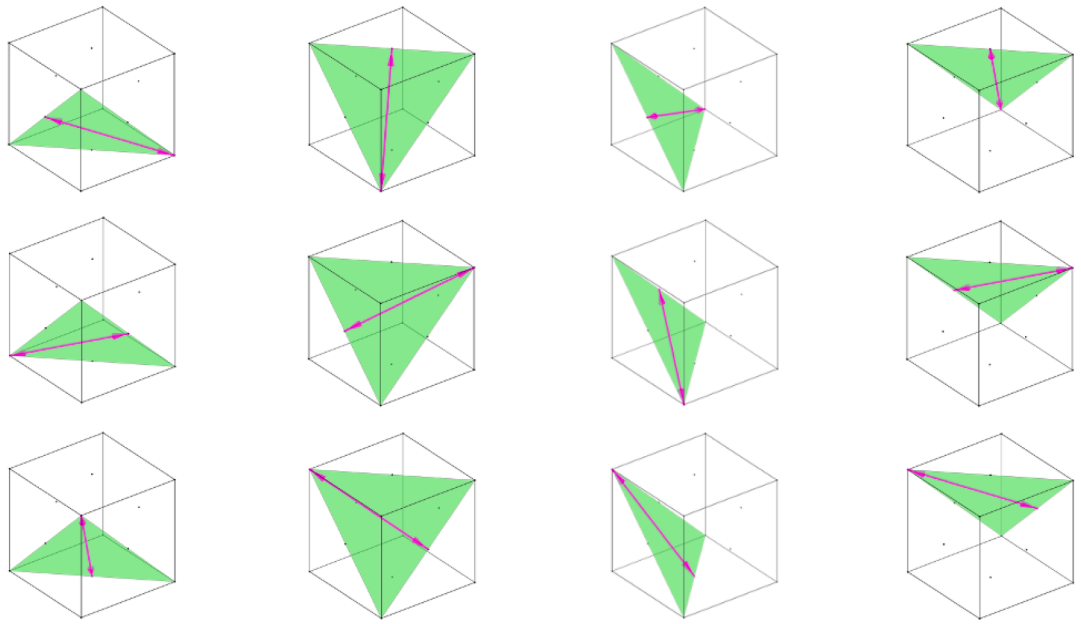

Fig. A1. Schematic illustration of the deformation twinning and martensitic phase transformation sytems in a FCC unit cell.

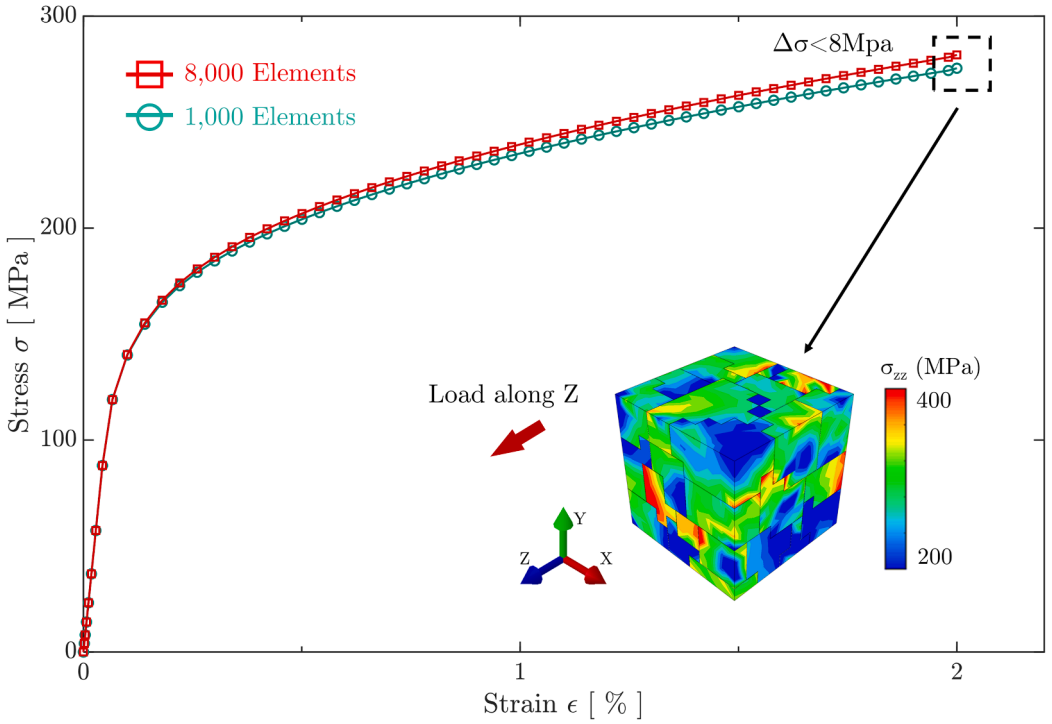

Fig. A2. Mesh sensitivty study on the calibration RVE.

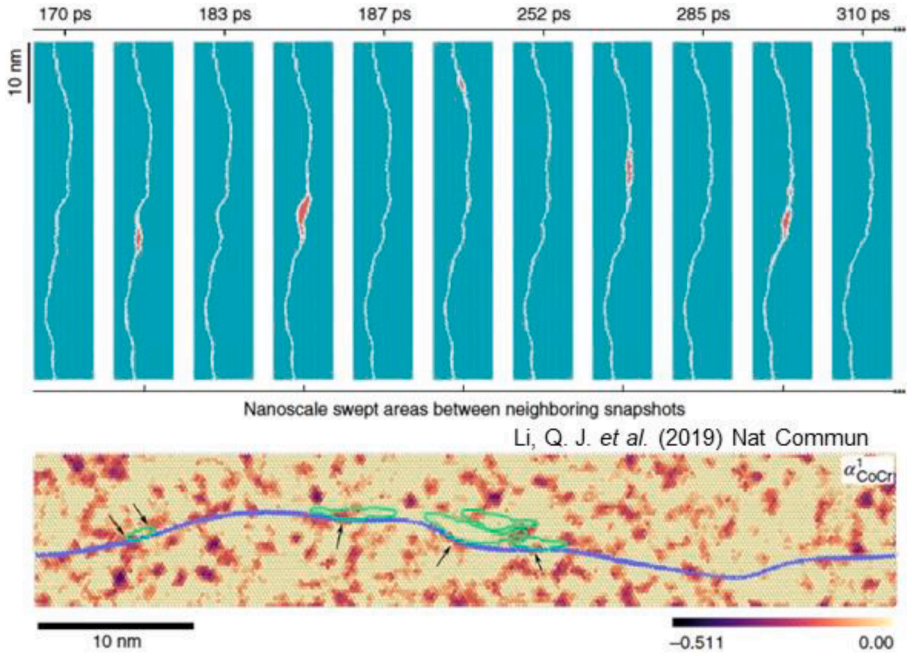

$$l_{\mathrm{SRO}} \cong v_{dis} \times \Delta t = \frac{5nm}{200ps} \times 10^{-6}s \approx 25\mu m$$

Fig. A3. The estimation of the length-scale of short-range order effect on the mechanical properties of MPEA, which is based on the dislocation gliding along lattices that were characterized by in-situ experiments.

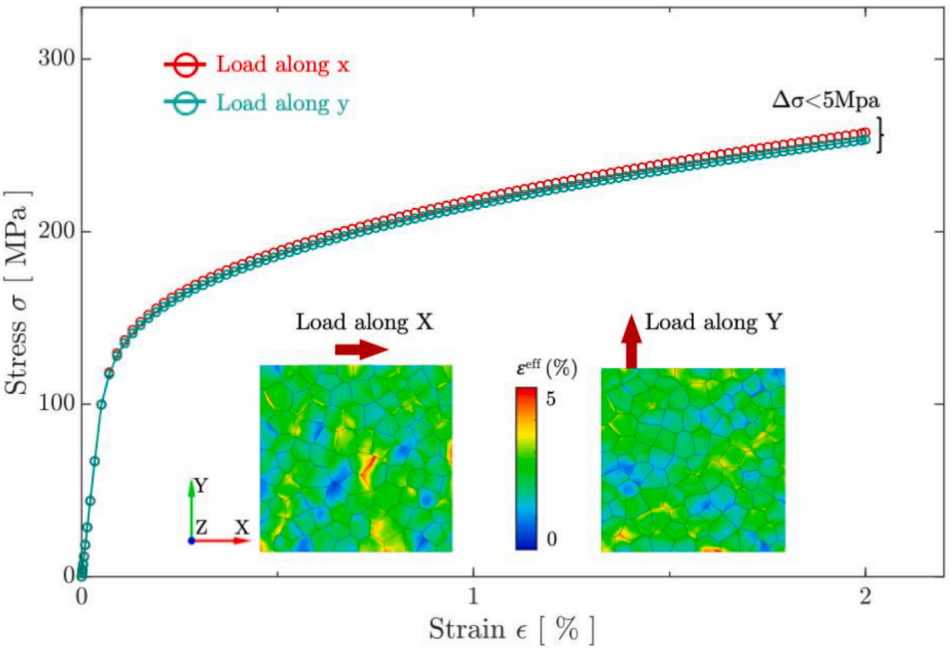

Fig. A4. The stress-strain responses of the RVE model used for cyclic loading analysis subject to the monotonic loadings along X and Y directions, respectively. The maximum discrepancy is limited up to 5 MPa (at strain level ϵ=2%), and hence the RVE is able to effectively capture and reflect the weak-textured microstructure features of the sample as shown in the experimental test (Liu et al., 2022).

References

Antillon, E., Woodward, C., Rao, S.I., Akdim, B., Parthasarathy, T.A., 2020. Chemical short range order strengthening in a model FCC high entropy alloy. Acta. Mater. 190, 29–42. https://doi.org/10.1016/j.actamat.2020.02.041.

Arsenlis, A., Parks, D.M., 1999. Crystallographic aspects of geometrically-necessary and statistically-stored dislocation density. Acta. Mater. 47, 1597–1611. https://doi.org/10.1016/S1359-6454(99)00020-8.

Benzerga, A.A., Brechet, Y., Needleman, A., Van der Giessen, E., 2005. The stored energy of cold work: predictions from discrete dislocation plasticity. Acta. Mater. 53, 4765–4779. https://doi.org/10.1016/j.actamat.2005.07.011.

Bergsmo, A., Xu, Y., Poole, B., Dunne, F.P.E., 2022. Twin boundary fatigue crack nucleation in a polycrystalline Nickel superalloy containing non-metallic inclusions. J. Mech. Phys. Solids 160. https://doi.org/10.1016/j.jmps.2022.104785.

Bu, Y., Wang, H., 2021. Short-range order in multicomponent alloys. Adv. Mech. 51, 915. https://doi.org/10.6052/1000-0992-21-027.

Cantor, B., 2021. Multicomponent high-entropy Cantor alloys. Prog. Mater. Sci. 120, 100754 https://doi.org/10.1016/j.pmatsci.2020.100754.

Cantor, B., Chang, I.T.H., Knight, P., Vincent, A.J.B., 2004. Microstructural development in equiatomic multicomponent alloys. Mat. Sci. Eng a-Struct. 375, 213–218. https://doi.org/10.1016/j.msea.2003.10.257.

Cao, FH., Wang, YJ., Dai, LH., 2020. Novel atomic-scale mechanism of incipient plasticity in a chemically complex CrCoNi medium-entropy alloy associated with inhomogeneity in local chemical environment. Acta. Mater. 194, 283–294. https://doi.org/10.1016/j.actamat.2020.05.042.

Cao, P., 2022. Maximum strength and dislocation patterning in multi–principal element alloys. Sci. Adv. 8, eabq7433. https://doi.org/10.1126/sciadv.abq7433.

Chen, B., Jiang, J., Dunne, F.P.E., 2018. Is stored energy density the primary meso-scale mechanistic driver for fatigue crack nucleation? Int. J. Plast. 101, 213–229. https://doi.org/10.1016/j.ijplas.2017.11.005.

Chen, S., Aitken, Z.H., Pattamatta, S., Wu, Z., Yu, Z.G., Srolovitz, D.J., Liaw, P.K., Zhang, Y.W., 2021a. Simultaneously enhancing the ultimate strength and ductility of high-entropy alloys via short-range ordering. Nat. Commun. 12, 4953. https://doi.org/10.1038/s41467-021-25264-5.

Chen, S., Wang, T., Li, X.Y., Cheng, Y., Zhang, G., Gao, H.J., 2022. Short-range ordering and its impact on thermodynamic property of high-entropy alloys. Acta. Mater. 238, 118201 https://doi.org/10.1016/j.actamat.2022.118201.

Chen, X., Wang, Q., Cheng, Z., Zhu, M., Zhou, H., Jiang, P., Zhou, L., Xue, Q., Yuan, F., Zhu, J., Wu, X., Ma, E., 2021b. Direct observation of chemical short-range order in a medium-entropy alloy. Nature 592, 712–716. https://doi.org/10.1038/s41586-021-03428-z.

Cheng, J., Ghosh, S., 2017. Crystal plasticity finite element modeling of discrete twin evolution in polycrystalline magnesium. J. Mech. Phys. Solids 99, 512–538. https://doi.org/10.1016/j.jmps.2016.12.008.

De Cooman, B.C., Estrin, Y., Kim, S.K., 2018. Twinning-induced plasticity (TWIP) steels. Acta. Mater. 142, 283–362. https://doi.org/10.1016/j.actamat.2017.06.046.

Ding, Q.Q., Fu, X.Q., Chen, D.K., Bei, H.B., Gludovatz, B., Li, J.X., Zhang, Z., George, E.P., Yu, Q., Zhu, T., Ritchie, R.O., 2019. Real-time nanoscale observation of deformation mechanisms in CrCoNi-based medium- to high-entropy alloys at cryogenic temperatures. Mater Today 25, 21–27. https://doi.org/10.1016/j.mattod.2019.03.001.

Dunne, F.P.E., Rugg, D., Walker, A., 2007. Lengthscale-dependent, elastically anisotropic, physically-based hcp crystal plasticity: application to cold-dwell fatigue in Ti alloys. Int. J. Plast. 23, 1061–1083. https://doi.org/10.1016/j.ijplas.2006.10.013.

Fang, Q.H., Lu, W.Z., Chen, Y., Feng, H., Liaw, P.K., Li, J., 2022. Hierarchical multiscale crystal plasticity framework for plasticity and strain hardening of multi-principal element alloys. J. Mech. Phys. Solids 169, 105067. https://doi.org/10.1016/j.jmps.2022.105067.

Gali, A., George, E.P., 2013. Tensile properties of high- and medium-entropy alloys. Intermetallics 39, 74–78. https://doi.org/10.1016/j.intermet.2013.03.018.

Galindo-Nava, E.I., 2017. On the prediction of martensite formation in metals. Scripta. Mater. 138, 6–11. https://doi.org/10.1016/j.scriptamat.2017.05.026.

George, E.P., Raabe, D., Ritchie, R.O., 2019. High-entropy alloys. Nat. Rev. Mater. 4, 515–534. https://doi.org/10.1038/s41578-019-0121-4.

Gludovatz, B., Hohenwarter, A., Catoor, D., Chang, E.H., George, E.P., Ritchie, R.O., 2014. A fracture-resistant high-entropy alloy for cryogenic applications. Science 345, 1153–1158. https://doi.org/10.1126/science.1254581.

Gludovatz, B., Hohenwarter, A., Thurston, K.V., Bei, H., Wu, Z., George, E.P., Ritchie, R.O., 2016. Exceptional damage-tolerance of a medium-entropy alloy CrCoNi at cryogenic temperatures. Nat. Commun. 7, 10602. https://doi.org/10.1038/ncomms10602.
Jian, W.R., Xie, Z.C., Xu, S.Z., Su, Y.Q., Yao, X.H., Beyerlein, I.J., 2020. Effects of lattice distortion and chemical short-range order on the mechanisms of deformation in medium entropy alloy CoCrNi. Acta. Mater. 199, 352–369. https://doi.org/10.1016/j.actamat.2020.08.044.
Jiang, J., Yang, J., Zhang, T.T., Dunne, F.P.E., Ben Britton, T., 2015. On the mechanistic basis of fatigue crack nucleation in Ni superalloy containing inclusions using high resolution electron backscatter diffraction. Acta. Mater. 97, 367–379. https://doi.org/10.1016/j.actamat.2015.06.035.
Kamlah, M., Haupt, P., 1997. On the macroscopic description of stored energy and self heating during plastic deformation. Int. J. Plast. 13, 893–911. https://doi.org/10.1016/S0749-6419(97)00063-6.
Karamitros, V., MacLachlan, D.W., Dunne, F.P.E., 2022. Mechanistic fatigue in Ni-based superalloy single crystals: a study of crack paths and growth rates. J. Mech. Phys. Solids 158, 104663. https://doi.org/10.1016/j.jmps.2021.104663.
Kawamura, M., Asakura, M., Okamoto, N.L., Kishida, K., Inui, H., George, E.P., 2021. Plastic deformation of single crystals of the equiatomic Cr-Mn-Fe-Co-Ni high-entropy alloy in tension and compression from 10K to 1273K. Acta. Mater. 203 https://doi.org/10.1016/j.actamat.2020.10.073.
Kumar, P., Michalek, M., Cook, D.H., Sheng, H., Lau, K.B., Wang, P., Zhang, M.W., Minor, A.M., Ramamurty, U., Ritchie, R.O., 2023. On the strength and fracture toughness of an additive manufactured CrCoNi medium-entropy alloy. Acta. Mater. 258, 119249 https://doi.org/10.1016/j.actamat.2023.119249.
Lam, T.N., Lee, S.Y., Tsou, N.T., Chou, H.S., Lai, B.H., Chang, Y.J., Feng, R., Kawasaki, T., Harjo, S., Liaw, P.K., Yeh, A.C., Li, M.J., Cai, R.F., Lo, S.C., Huang, E.W., 2020. Enhancement of fatigue resistance by overload-induced deformation twinning in a CoCrFeMnNi high-entropy alloy. Acta. Mater. 201, 412–424. https://doi.org/10.1016/j.actamat.2020.10.016.
Laplanche, G., Bonneville, J., Varvenne, C., Curtin, W.A., George, E.P., 2018. Thermal activation parameters of plastic flow reveal deformation mechanisms in the CrMnFeCoNi high-entropy alloy. Acta. Mater. 143, 257–264. https://doi.org/10.1016/j.actamat.2017.10.014.
Laplanche, G., Gadaud, P., Horst, O., Otto, F., Eggeler, G., George, E.P., 2015. Temperature dependencies of the elastic moduli and thermal expansion coefficient of an equiatomic, single-phase CoCrFeMnNi high-entropy alloy. J. Alloys Compd. 623, 348–353. https://doi.org/10.1016/j.jallcom.2014.11.061.
Laplanche, G., Kostka, A., Horst, O.M., Eggeler, G., George, E.P., 2016. Microstructure evolution and critical stress for twinning in the CrMnFeCoNi high-entropy alloy. Acta. Mater. 118, 152–163. https://doi.org/10.1016/j.actamat.2016.07.038.
Li, C., Cao, F.H., Chen, Y., Wang, H.Y., Dai, L.H., 2022a. Crystal plasticity model analysis of the effect of short-range order on strength-plasticity of medium entropy alloys. Metals 12. https://doi.org/10.3390/met12101757.
Li, J., Chen, Y., He, Q., Xu, X., Wang, H., Jiang, C., Liu, B., Fang, Q., Liu, Y., Yang, Y., Liaw, P.K., Liu, C.T., 2022b. Heterogeneous lattice strain strengthening in severely distorted crystalline solids. Proc. Natl. Acad. Sci. U S A 119, e2200607119. https://doi.org/10.1073/pnas.2200607119.
Li, Q.J., Sheng, H., Ma, E., 2019a. Strengthening in multi-principal element alloys with local-chemical-order roughened dislocation pathways. Nat. Commun. 10, 3563. https://doi.org/10.1038/s41467-019-11464-7.
Li, W., Chen, S., Aitken, Z., Zhang, YW., 2023. Shock-induced deformation and spallation in CoCrFeMnNi high-entropy alloys at high strain-rates. Int. J. Plast. 168, 103691 https://doi.org/10.1016/j.ijplas.2023.103691.
Li, Z., Pradeep, K.G., Deng, Y., Raabe, D., Tasan, C.C., 2016. Metastable high-entropy dual-phase alloys overcome the strength–ductility trade-off. Nature 534, 227–230. https://doi.org/10.1038/nature17981.
Li, Z.Z., Zhao, S.T., Ritchie, R.O., Meyers, M.A., 2019b. Mechanical properties of high-entropy alloys with emphasis on face-centered cubic alloys. Prog. Mater. Sci. 102, 296–345. https://doi.org/10.1016/j.pmatsci.2018.12.003.
Liu, D., Yu, Q., Kabra, S., Jiang, M., Forna-Kreutzer, P., Zhang, R., Payne, M., Walsh, F., Gludovatz, B., Asta, M., Minor, A.M., George, E.P., Ritchie, R.O., 2022. Exceptional fracture toughness of CrCoNi-based medium- and high-entropy alloys at 20 kelvin. Science 378, 978–983. https://doi.org/10.1126/science.abp8070.
Long, D.J., Dunne, F.P.E., 2023. On the mechanistic driving force for short fatigue crack path. J. Mech. Phys. Solids 179, 105368. https://doi.org/10.1016/j.jmps.2023.105368.
Lu, K.J., Chauhan, A., Litvinov, D., Schneider, M., Laplanche, G., Aktaa, J., 2023. Cooperative deformation mechanisms in a fatigued CoCrNi multi-principal element alloy: a case of low stacking fault energy. J. Mech. Phys. Solids 180, 105419. https://doi.org/10.1016/j.jmps.2023.105419.
Lu, X., Dunne, F.P.E., Xu, Y., 2020a. A crystal plasticity investigation of slip system interaction, GND density and stored energy in non-proportional fatigue in Nickel-based superalloy. Int. J. Fatigue 139, 105782. https://doi.org/10.1016/j.ijfatigue.2020.105782.
Lu, X.C., Zhang, X., Shi, M.X., Roters, F., Kang, G.Z., Raabe, D., 2019. Dislocation mechanism based size-dependent crystal plasticity modeling and simulation of gradient nano-grained copper. Int. J. Plast. 113, 52–73. https://doi.org/10.1016/j.ijplas.2018.09.007.
Lu, X.C., Zhao, J.F., Yu, C., Li, Z.M., Kan, Q.H., Kang, G.Z., Zhang, X., 2020b. Cyclic plasticity of an interstitial high-entropy alloy: experiments, crystal plasticity modeling, and simulations. J. Mech. Phys. Solids 142, 103971. https://doi.org/10.1016/j.jmps.2020.103971.
Mecking, H., Kocks, U.F., 1981. Kinetics of flow and strain-hardening. Acta. Metallurg. 29, 1865–1875. https://doi.org/10.1016/0001-6160(81)90112-7.
Ming, K.S., Lu, W.J., Li, Z.M., Bi, X.F., Wang, J., 2020. Amorphous bands induced by low temperature tension in a non-equiatomic CrMnFeCoNi alloy. Acta. Mater. 188, 354–365. https://doi.org/10.1016/j.actamat.2020.02.024.
Naeem, M., He, H., Zhang, F., Huang, H., Harjo, S., Kawasaki, T., Wang, B., Lan, S., Wu, Z., Wang, F., Wu, Y., Lu, Z., Zhang, Z., Liu, C.T., Wang, X.L., 2020. Cooperative deformation in high-entropy alloys at ultralow temperatures. Sci. Adv. 6, eaax4002. https://doi.org/10.1126/sciadv.aax4002.
Niu, C., LaRosa, C.R., Miao, J., Mills, M.J., Ghazisaeidi, M., 2018. Magnetically-driven phase transformation strengthening in high entropy alloys. Nat. Commun. 9, 1363. https://doi.org/10.1038/s41467-018-03846-0.
Otto, F., Dlouhy, A., Somsen, C., Bei, H., Eggeler, G., George, E.P., 2013. The influences of temperature and microstructure on the tensile properties of a CoCrFeMnNi high-entropy alloy. Acta. Mater. 61, 5743–5755. https://doi.org/10.1016/j.actamat.2013.06.018.
Prastiti, N.G., Xu, Y., Balint, D.S., Dunne, F.P.E., 2020. Discrete dislocation, crystal plasticity and experimental studies of fatigue crack nucleation in single-crystal nickel. Int. J. Plast. 126, 102615 https://doi.org/10.1016/j.ijplas.2019.10.003.
Qian, H., Huang, Z., Fan, H., Wang, Y., Cao, L., Zhu, Q., Zhao, C., 2023. Fatigue behaviour analysis of thermal cyclic loading for through-silicon via structures based on backstress stored energy density. Int. J. Fatigue, 107978. https://doi.org/10.1016/j.ijfatigue.2023.107978.
Rao, S.I., Woodward, C., Parthasarathy, T.A., Senkov, O., 2017. Atomistic simulations of dislocation behavior in a model FCC multicomponent concentrated solid solution alloy. Acta. Mater. 134, 188–194. https://doi.org/10.1016/j.actamat.2017.05.071.
Roters, F., Eisenlohr, P., Hantcherli, L., Tjahjanto, D.D., Bieler, T.R., Raabe, D., 2010. Overview of constitutive laws, kinematics, homogenization and multiscale methods in crystal plasticity finite-element modeling: theory, experiments, applications. Acta. Mater. 58, 1152–1211. https://doi.org/10.1016/j.actamat.2009.10.058.
Sangid, M.D., 2013. The physics of fatigue crack initiation. Int. J. Fatigue 57, 58–72. https://doi.org/10.1016/j.ijfatigue.2012.10.009.
Sangid, M.D., Maier, H.J., Sehitoglu, H., 2011. The role of grain boundaries on fatigue crack initiation - An energy approach. Int. J. Plast. 27, 801–821. https://doi.org/10.1016/j.ijplas.2010.09.009.
Suresh, S., 2012. Fatigue of Materials, 2 ed. Cambridge University Press, Cambridge.
Tirunilai, A.S., Hanemann, T., Weiss, K.P., Freudenberger, J., Heilmaier, M., Kauffmann, A., 2020. Dislocation-based serrated plastic flow of high entropy alloys at cryogenic temperatures. Acta. Mater. 200, 980–991. https://doi.org/10.1016/j.actamat.2020.09.052.
Tracy, C.L., Park, S., Rittman, D.R., Zinkle, S.J., Bei, H., Lang, M., Ewing, R.C., Mao, W.L., 2017. High pressure synthesis of a hexagonal close-packed phase of the high-entropy alloy CrMnFeCoNi. Nat. Commun. 8, 15634. https://doi.org/10.1038/ncomms15634.
Wagner, C., Laplanche, G., 2023. Effect of grain size on critical twinning stress and work hardening behavior in the equiatomic CrMnFeCoNi high-entropy alloy. Int. J. Plast. 166, 103651 https://doi.org/10.1016/j.ijplas.2023.103651.
Wan, V.V.C., MacLachlan, D.W., Dunne, F.P.E., 2014. A stored energy criterion for fatigue crack nucleation in polycrystals. Int. J. Fatigue 68, 90–102. https://doi.org/10.1016/j.ijfatigue.2014.06.001.
Wan, W., Xu, Y., Yu, X., Dunne, F.P.E., 2023. Microstructurally-sensitive fatigue crack nucleation in a Zircaloy-4 alloy. J. Mech. Phys. Solids 180, 105417. https://doi.org/10.1016/j.jmps.2023.105417.

Warner, D.H., Curtin, W.A., Qu, S., 2007. Rate dependence of crack-tip processes predicts twinning trends in f.c.c. metals. Nat. Mater. 6, 876–881. https://doi.org/10.1038/nmat2030.

Wong, S.L., Madivala, M., Prahl, U., Roters, F., Raabe, D., 2016. A crystal plasticity model for twinning- and transformation-induced plasticity. Acta. Mater. 118, 140–151. https://doi.org/10.1016/j.actamat.2016.07.032.

Woo, W., Kim, Y.S., Chae, H.B., Lee, S.Y., Jeong, J.S., Lee, C.M., Won, J.W., Na, Y.S., Kawasaki, T., Harjo, S., An, K., 2023. Competitive strengthening between dislocation slip and twinning in cast-wrought and additively manufactured CrCoNi medium entropy alloys. Acta. Mater. 246, 118699 https://doi.org/10.1016/j.actamat.2023.118699.

Wu, H., Fan, G., 2020. An overview of tailoring strain delocalization for strength-ductility synergy. Prog. Mater. Sci. 113, 100675 https://doi.org/10.1016/j.pmatsci.2020.100675.

Wu, X.L., 2023. Chemical short-range orders in high-/medium-entropy alloys. J. Mater. Sci. Technol. 147, 189–196. https://doi.org/10.1016/j.jmst.2022.10.070.

Xie, D., Feng, R., Liaw, P.K., Bei, H.B., Gao, Y.F., 2020. Tensile creep behavior of an equiatomic CoCrNi medium entropy alloy. Intermetallics 121, 106775. https://doi.org/10.1016/j.intermet.2020.106775.

Xu, Y., 2021. A non-local methodology for geometrically necessary dislocations and application to crack tips. Int. J. Plast. 140, 102970 https://doi.org/10.1016/j.ijplas.2021.102970.

Xu, Y., Gu, T., Xian, J., Giuliani, F., Ben Britton, T., Gourlay, C.M., Dunne, F.P.E., 2021a. Intermetallic size and morphology effects on creep rate of Sn-3Ag-0.5Cu solder. Int. J. Plast. 137, 102904 https://doi.org/10.1016/j.ijplas.2020.102904.

Xu, Y., Wan, W., Dunne, F.P.E., 2021b. Microstructural fracture mechanics: stored energy density at fatigue cracks. J. Mech. Phys. Solids 146, 104209. https://doi.org/10.1016/j.jmps.2020.104209.

Xu, Y., Worsnop, F.F., Dye, D., Dunne, F.P.E., 2023. Slip intermittency and dwell fatigue in titanium alloys: a discrete dislocation plasticity analysis. J. Mech. Phys. Solids 179, 105384. https://doi.org/10.1016/j.jmps.2023.105384.

Xu, Y., Xian, J., Stoyanov, S., Bailey, C., Coyle, R.J., Gourlay, C.M., Dunne, F.P.E., 2022. A multi-scale approach to microstructure-sensitive thermal fatigue in solder joints. Int. J. Plast. 155, 103308 https://doi.org/10.1016/j.ijplas.2022.103308.

Zepeda-Ruiz, L.A., Stukowski, A., Oppelstrup, T., Bulatov, V.V., 2017. Probing the limits of metal plasticity with molecular dynamics simulations. Nature 550, 492–495. https://doi.org/10.1038/nature23472.

Zhang, F., Wu, Y., Lou, H., Zeng, Z., Prakapenka, V.B., Greenberg, E., Ren, Y., Yan, J., Okasinski, J.S., Liu, X., Liu, Y., Zeng, Q., Lu, Z., 2017. Polymorphism in a high-entropy alloy. Nat. Commun. 8, 15687. https://doi.org/10.1038/ncomms15687.

Zhang, M.W., Yu, Q., Frey, C., Walsh, F., Payne, M.I., Kumar, P., Liu, D.Y., Pollock, T.M., Asta, M.D., Ritchie, R.O., Minor, A.M., 2022a. Determination of peak ordering in the CrCoNi medium-entropy alloy via nanoindentation. Acta. Mater 241. https://doi.org/10.1016/j.actamat.2022.118380.

Zhang, R., Zhao, S., Ding, J., Chong, Y., Jia, T., Ophus, C., Asta, M., Ritchie, R.O., Minor, A.M., 2020. Short-range order and its impact on the CrCoNi medium-entropy alloy. Nature 581, 283–287. https://doi.org/10.1038/s41586-020-2275-z.

Zhang, X., Lu, X.C., Zhao, J.F., Kan, Q.H., Li, Z.M., Kang, G.Z., 2022b. Temperature effect on tensile behavior of an interstitial high entropy alloy: crystal plasticity modeling. Int. J. Plast. 150 https://doi.org/10.1016/j.ijplas.2021.103201.

Zhang, X.X., Stinville, J.C., Pollock, T.M., Dunne, F.P.E., 2021. Crystallography and elastic anisotropy in fatigue crack nucleation at nickel alloy twin boundaries. J. Mech. Phys. Solids 155. https://doi.org/10.1016/j.jmps.2021.104538.

Zhang, Y., Zuo, T.T., Tang, Z., Gao, M.C., Dahmen, K.A., Liaw, P.K., Lu, Z.P., 2014. Microstructures and properties of high-entropy alloys. Prog. Mater Sci. 61, 1–93. https://doi.org/10.1016/j.pmatsci.2013.10.001.

Zhang, Z., Dunne, F.P.E., 2017. Microstructural heterogeneity in rate-dependent plasticity of multiphase titanium alloys. J. Mech. Phys. Solids 103, 199–220. https://doi.org/10.1016/j.jmps.2017.03.012.

Zhang, Z., Mao, M.M., Wang, J., Gludovatz, B., Zhang, Z., Mao, S.X., George, E.P., Yu, Q., Ritchie, R.O., 2015. Nanoscale origins of the damage tolerance of the high-entropy alloy CrMnFeCoNi. Nat. Commun. 6, 10143. https://doi.org/10.1038/ncomms10143.

Zheng, Z.B., Prastiti, N.G., Balint, D.S., Dunne, F.P.E., 2019. The dislocation configurational energy density in discrete dislocation plasticity. J. Mech. Phys. Solids 129, 39–60. https://doi.org/10.1016/j.jmps.2019.04.015.